Geophysical estimation of shallow permafrost distribution and properties in an ice-wedge polygon-dominated Arctic tundra region

Baptiste Dafflon[1], Susan Hubbard[1], Craig Ulrich[1], John Peterson[1], Yuxin Wu[1], Haruko Wainwright[1], and Timothy J. Kneafsey[1]

[1] Lawrence Berkeley National Laboratory, Earth Science Division, Berkeley, California, USA. E-mail: bdafflon@lbl.gov; sshubbard@lbl.gov; culrich@lbl.gov; jepeterson@lbl.gov; ywu3@lbl.gov; hmwainwright@lbl.gov; tjkneafsey@lbl.gov.

Abstract

Shallow permafrost distribution and characteristics are important for predicting ecosystem feedbacks to a changing climate over decadal to century timescales because they can drive active layer deepening and land surface deformation, which in turn can significantly affect hydrologic and biogeochemical responses, including greenhouse gas dynamics. As part of the U.S. Department of Energy Next-Generation Ecosystem Experiments-Arctic, we have investigated shallow Arctic permafrost characteristics at a site in Barrow, Alaska, with the objective of improving our understanding of the spatial distribution of shallow permafrost, its associated properties, and its links with landscape microtopography. To meet this objective, we have acquired and integrated a variety of information, including electric resistance tomography data, frequency-domain electromagnetic induction data, laboratory core analysis, petrophysical studies, high-resolution digital surface models, and color mosaics inferred from kite-based landscape imaging. The results of our study provide a comprehensive and high-resolution examination of the distribution and nature of shallow permafrost in the Arctic tundra, including the estimation of ice content, porosity, and salinity. Among other results, porosity in the top 2 m varied between 85% (besides ice wedges) and 40%, and was negatively correlated with fluid salinity. Salinity directly influenced ice and unfrozen water content and indirectly influenced the soil organic matter content. A relatively continuous but depth-variable increase in salinity led to a partially unfrozen saline layer (cryopeg) located below the top of the permafrost. The cryopeg environment could lead to year-round microbial production of greenhouse gases. Results also indicated a covariability between topography and permafrost characteristics including icewedge and salinity distribution. In addition to providing insight about the Arctic ecosystem, through integration of lab-based petrophysical results with field data, this study also quantified the key controls on electric resistivity at this Arctic permafrost site, including salinity, porosity, water content, ice content, soil organic matter content, and lithologic properties.

INTRODUCTION

The Arctic is a region that is particularly sensitive to climate warming, and Arctic ecosystem feedbacks to climate are a significant source of uncertainty

in climate projections (e.g., Friedlingstein et al., 2006; Koven et al., 2011). The northern circumpolar permafrost soil is particularly important to quantify feedbacks to a warming climate because it contains a vast pool of carbon currently locked up in frozen permafrost (1672 Pg; Tarnocai et al., 2009) and because microbial decomposition of organic-rich thawing permafrost may lead to a significant increase in CO_2 and CH_4 production (e.g., Schaphoff et al., 2013). Permafrost thaw can also directly influence numerous components of the terrestrial ecosystem, including energy balance, vegetation dynamics, hydrologic processes, coastal erosion, and land surface deformation (e.g., Hinzman et al., 2005; Schaefer et al., 2012).

Permafrost, which is present on approximately 23% of the exposed land in the northern hemisphere, is defined as earth material having a temperature colder than 0°C for two or more years (Washburn, 1979; Jorgenson, 2011). Unlike the active layer, which represents the upper horizons of soil in permafrost regions that thaws seasonally due to climatic variations, permafrost remains frozen throughout the year. An exception to the frozen permafrost is saline-rich permafrost, in which freezing-point depression can lead to unfrozen permafrost layers even at temperatures colder than 0°C, a situation referred to as saline permafrost or cryopeg.

Gaining a predictive understanding of Arctic ecosystem dynamics and evolution requires quantification of the active layer and the permafrost and their interactions. Although numerous studies have investigated active-layer processes, including gradual deepening due to climate warming (e.g., Hinzman et al., 1991; Hinkel and Nelson, 2003; Engstrom et al., 2005; Hubbard et al., 2013), only a limited number of studies have focused on exploring how shallow permafrost contributes to the functioning and evolution of a terrestrial ecosystem (Romanovsky and Osterkamp, 2001; Jorgenson et al., 2010; Michaelson et al., 2011). Most of the existing permafrost ecosystem studies have focused on assessing shallow permafrost soil organic matter content (Bockheim, 2007; Ping et al., 2008; Hugelius et al., 2014) and their relationship to permafrost properties. For example, Bockheim et al. (1999) find that variations in soil organic carbon content varied strongly with the amount of ground ice (Bockheim et al., 1999), and Michaelson et al. (2011) find a significant correlation between carbon dioxide gas content and permafrost ice content. Other studies focus on investigating specific permafrost properties, such as ground ice characteristics, salinity, thermal properties, and soil cryostructure (Mackay, 2000; Romanovsky and Osterkamp, 2000; Kanevskiy et al., 2013) and how these properties can drive different rates in active layer deepening, thaw settlement, soil subsidence, coastal erosion, and ice-wedge growth or degradation (e.g., Washburn, 1980; Romanovsky and Osterkamp, 2000; Pullman et al., 2007).

Although less emphasized in the literature, permafrost properties can also have a significant impact on ecosystem function, particularly through their control on microtopography. In low-gradient environments, such as the Arctic tundra, microtopography can significantly influence active layer hydrologic

storage capacity and drainage (e.g., Engstrom et al., 2005). Microtopography-influenced changes in active layer hydrology can in turn influence a cascade of processes that influence Arctic terrestrial feedbacks to climate, including thermal processes, energy balance, vegetation, microbial respiration, and the associated CO_2 and CH_4 fluxes (Jorgenson et al., 2010).

Beyond the potential influence of permafrost evolution on microtopography and thus active-layer processes, microbial degradation of organic carbon occurring within permafrost layers is also of interest and understudied. Microbial activity has been documented in the permafrost, even in the presence of a small amount of unfrozen water surrounding soil grains and under saline and subzero temperature conditions (Gilichinsky et al., 2005; Shcherbakova et al., 2005, 2009; Pecheritsyna et al., 2007). Because saline permafrost has been observed at many locations in northern regions (e.g., Hivon and Sego, 1993; Brouchkov, 2002; Hubbard et al., 2013) and it is expected to be widespread in coastal regions (Brouchkov, 2003), documenting the nature and distribution of saline permafrost and its particular control on microbial degradation of organic carbon to overall ecosystem CO_2 and CH_4 fluxes could be important for the evolving Arctic region.

In spite of the potential importance of shallow permafrost on civil infrastructure and ecosystem evolution, poor characterization of shallow permafrost systems in sufficiently high resolution and over landscape-relevant scales has limited an assessment of its distribution, nature, and influences on the ecosystem. The objective of this study is to use geophysical approaches with core-based petrophysical analysis to characterize shallow permafrost (the top 5 m below the ground surface) properties, including its salinity, porosity, and ice content. A major advance compared with previous studies investigating such permafrost properties in the Arctic (e.g., Yoshikawa et al., 2004; Kanevskiy et al., 2013) is the use of geophysical and core samples analysis to investigate soil properties' covariability and petrophysical relationships, which enables estimation of the spatial distribution of these soil properties. In addition, geophysical data are used with digital surface models to quantify the covariation between permafrost and landscape properties. Our study is conducted in Barrow, Alaska, an ice-wedge polygon-rich Arctic tundra environment, as part of the U.S. Department of Energy (DOE) Next-Generation Ecosystem Experiments (NGEE Arctic). NGEE Arctic aims to develop a process-rich ecosystem model to simulate the evolution of the Arctic ecosystem in a changing climate.

This paper is organized as follows: We provide a background on the geophysical and landscape imaging approaches. We also present the study site and discuss previous studies that have been conducted there to characterize the permafrost. Furthermore, we describe data processing and petrophysical models adapted to the specificities of the studied environment. Finally, we present and discuss the results of the geophysical investigation

and core-based analysis and the covariance between the permafrost and landscape geomorphic features.

BACKGROUND: GEOPHYSICAL AND LANDSCAPE IMAGING APPROACHES

In this study, we investigate the top 5 m of the Barrow subsurface using a variety of data sets and information. We focus on the use of electric and electromagnetic geophysical methods that are sensitive to electric conductivity (EC) distribution of the subsurface. To constrain and interpret the electric resistivity tomographic and electromagnetic data, we have used information available from cores, petrophysical relationships, and a digital surface elevation model (DSM), and a red-green-blue (RGB) color mosaic inferred from low-altitude aerial imaging.

The electric resistivity tomography (ERT) method, which normally requires galvanic contact (e.g., electrodes inserted into the ground), is commonly used to obtain relatively high spatial resolution estimates of shallow subsurface EC distribution by applying an inversion method on the acquired resistance data (e.g., LaBrecque et al., 1996; Kemna, 2000; Binley and Kemna, 2005; Karaoulis et al., 2011; Johnson et al., 2012). The ERT approach has been applied widely to investigate the spatial and temporal distribution of EC in permafrost systems, in alpine (e.g., Hauck, 2002; Krautblatter et al., 2010) and in Arctic environments (e.g., Yoshikawa et al., 2006; Hubbard et al., 2013). ERT surveys in an Arctic environment enabled investigators to characterize the spatial distribution of various lithologic units (Yoshikawa et al., 2004), to estimate active layer properties (Hubbard et al., 2013), to estimate water content in permafrost (Fortier et al., 2008), and to investigate the dynamics of freeze-thaw processes and water-to-ice transitions (Overduin et al., 2012; Wu et al., 2013).

In comparison with galvanically coupled electric methods, portable electromagnetic induction (EMI) tools do not require contact with the ground and can be used to acquire subsurface apparent EC variations with one-person operation (e.g., Keller and Frischknecht, 1966; McNeill, 1990; Everett and Meju, 2005). Different depth sensitivity functions are obtained by changing the configuration of the instrument with regard to the coil spacing, orientation, elevation above the ground surface, and signal frequency. The most common application of one-person-operated frequency-domain EMI instruments is mapping near-surface lateral variability in apparent EC, which provides one estimate of EC over the depth interval of investigation (e.g., Corwin and Lesch, 2005; Quinn et al., 2010). Using different coil configurations, several approaches have been developed to also estimate the vertical distribution of EC from EMI data (e.g., Farquharson et al., 2003; Dafflon et al., 2013). The major critical issue with near-surface EMI imaging using data collected with portable tools is the nonuniqueness of the solution, which is caused by the limited number of measurements at each location and the sometimes poor diversity in the depth sensitivity function of various tool configurations (Dafflon et al., 2013).

High-resolution and georeferenced landscape images and DSM were used in this study to explore in detail the relationships between permafrost characteristics and geomorphology. At the local scale, the use of aircraft-based technology for acquiring such data can be very expensive. An alternative approach of increasing interest is the use of unmanned aerial systems (e.g., kite, balloon, or unmanned aircraft vehicle) as a platform at low altitude to acquire numerous images (e.g., using a three-channel color camera, a nearinfrared camera, and a thermal camera). Recent developments of powerful automated feature extraction and bundle adjustment algorithms based on the structure-from-motion technique enable reconstruction of DSM and multispectral orthomosaics (e.g., James and Robson, 2012). In earth sciences, reconstruction of orthomosaic and/or DSM from a light unmanned aerial system has been recently used for various purposes, such as geomorphic studies (e.g., James and Robson, 2012; Bryson et al., 2013) and vegetation inventory and monitoring (e.g., Berni et al., 2009; Dandois and Ellis, 2013).

STUDY SITE AND PREVIOUS PERMAFROST STUDIES NEAR SITE

The study site (Figure 1) is located within the Barrow Environmental Observatory near the village of Barrow on the Alaskan Arctic Coastal Plain, approximately 4 mi from the Beaufort Sea. The landscape at the site has a low topographic relief varying between 2 and 6 m in elevation, and it is dominated by different types of polygons, including high-, low-, and flat-centered (e.g., Hinkel et al., 2001; Hubbard et al., 2013). Polygon geomorphology governs the microtopography, whereas larger trends in topography are driven by depositional process, ice accumulation, landscape uplift, drainage network, formation of thaw lakes, and presence of drained thaw lake basins (Sellmann et al., 1975).

The permafrost at this site is generally considered to be perennially frozen down to depths of 300–400 m (e.g., Sellmann et al., 1975). The depth of the 0° seasonal amplitude (the depth at which the temperature stays constant over the year) at Barrow is approximately 16 m (Yoshikawa et al., 2004), and the temperature at that depth is approximately −9°C. From 0 to 16 m below the ground surface, the seasonal temperature variation decreases gradually. Figure 2 shows a temperature depth profile between 0 and 3 m at the NGEE site (courtesy of V. Romanovsky, UAF) for each month between October 2012 and October 2013. The temperature near the surface fluctuates between –22°C and 5°C, whereas at a 3-m depth, the temperature fluctuates between –12°C and –5°C. The thickness of the seasonally thawed active layer at the site is generally less than 0.5 m (e.g., Shiklomanov et al., 2010; Goswami et al., 2011), and it depends primarily on the soil texture, water content, water inundation, and seasonal temperature variations (Hubbard et al., 2013).

The sediments underlying the active layer consist of a mixture of sand, gravel, and silt. These sediments, of marine origin, are part of the Gubik

Formation of the Arctic Coastal Plain. This formation is largely the product of various marine transgressions generally involving the near-shore shelf depositional environment (Black, 1964) with the most recent occurrence in Mid-Wisconsinan time (Sellmann et al., 1975; Brown et al., 1980). The upper part of the Gubik Formation is known as the Barrow unit, which Black (1964) describes as a few tens of feet thick (top 3–6 m) and generally of marine origin at the base, with the uppermost sediments characterized by lacustrine and fluvial deposits. Postdepositional freezing occurred in several steps, likely after a process known as soil water freshening, in which pore water present at the time of deposition is replaced by other fluids. Thus, the shallow subsurface has been influenced by marine deposits and alluvial, lacustrine, eolian, and cryogenic processes (Meyer et al., 2010). This upper permafrost structure has been further influenced by polygonal ground and ice-wedge development over many thousands of years (Leffingwell, 1915; Lachenbruch, 1962). As such, the upper permafrost soil is likely to have significant spatial variability in terms of sediment type, organic content, ice structures, and salinity.

Documented using primarily core data sets, the volume of shallow ground ice around Barrow is high, with values commonly up to 80% (e.g., Brown and Sellmann, 1973; Kanevskiy et al., 2013). The ground ice at Barrow is predominantly associated with ice wedges and soil cryogenic structures including segregated and pore ice (e.g., Kanevskiy et al., 2013). Soil cryogenic structures in this region can be ataxitic (suspended soil in ice), reticulate, layered, crustal, porous, or organic matrix (e.g., Kanevskiy et al., 2013). These patterns are caused by different processes, including repeated freezing and thawing, cryoturbation, frost heave, and soil accumulation, which together can lead to a much higher total porosity in frozen soil than in unfrozen soils. A second source of ground ice in this region is ice wedges, which are the result of repeated thermal cracking processes caused by soil contraction during cold periods and water infiltration during the growing season (Leffingwell, 1915; Mackay, 2000). Here, we use a simple but widely used classification of ice-wedge-based topography, in which we categorize various stages of ice-wedge landscape features, such as low-centered polygons (LCPs), flat-centered polygons (FCPs) (also called transitional or intermediate in other studies), and high-centered polygons (HCPs). LCP generally refers to the ice-wedge aggrading stage, whereas HCP refers to stable or partly degraded wedges. However, classifying the ice-wedge stage is difficult because primary wedges are complemented by secondary and tertiary ice wedges that formed later and tend to increase fractality and decrease the size of polygons (e.g., Mackay, 2000).

Several studies confirm that the ice content in the permafrost around Barrow is very high in the upper part and decreases with depth (Brown et al., 1980). Kanevskiy et al. (2013) quantify the ground ice distribution and volume in the shallow permafrost (top 2–3 m) based on 339 core samples obtained from 65 sites distributed along the Beaufort Sea from Point Barrow to the

Canadian border. They calculate the segregated and pore ice content for all samples, and they calculate the average ice-wedge volume over an associated 100 × 100 m^2 area using a parametric relationship between the average polygon size and the estimated ice-wedge widths. Among other results, they report for the coastal plain an average total ice content (i.e., ice wedge, segregated, and pore ice) of 83% and 82% for the primary surface (deposits not reworked by recent lacustrine processes and often covered with polygonshaped landscape) and for the drained-lakes basins, respectively. For the primary surface of the coastal plain, they estimate that the portion of frozen soil with an ataxitic cryostructure is 50%, the volume of the pore and segregated ice is 80%, and the ice-wedge average volume is 13% (ranging from 4% to 28%). Old drained thaw lake basins show trends relatively similar to the primary surface, whereas younger ones show lower ice content.

Another aspect of permafrost in Barrow, and in many coastal regions in the Arctic (Brouchkov, 2002, 2003), is the presence of some partially unfrozen permafrost due to the elevated soil salinity. Around Barrow, saline layers or lenses have been observed at different investigation sites and at various depths, with a generally progressive increase in salinity with depth (e.g., O'Sullivan, 1966; Brown, 1969a; Williams, 1970; Yoshikawa et al., 2004). High but variable ionic concentration values have been observed in numerous core samples at 3–6 m in depth (O'Sullivan, 1966; Brown, 1969b; Sellmann et al., 1975) with some salinity values at 0.5, one, and two times the seawater salinity at depths of 2.15, 4.3, and 5.2 m depth, respectively, but with only rare occurrences of flowing brine at these depths (O'Sullivan, 1966). O'Sullivan explains some of the strong lateral variability between different locations as resulting from the local influence of permafrost deformation and ice segregation on heterogeneity, the texture of sediments, and the successive freezing processes.

The EC of the permafrost at Barrow has been documented to be unexpectedly high, possibly due to unfrozen conditions, saline conditions, or both. Geophysical investigations (Yoshikawa et al., 2004) report a bulk resistivity of 20 ohm-m below 1.8 m in depth and as low as 8.1 ohm-m at a 33.5-m depth in which brine flowing in well was observed. Their study also reports that the freezing point of a brine sample from 31.5 m in depth was about equal to the ground temperature in this 0° seasonal amplitude zone (−9.4°C), thus indicating that the upper part of the saline layer of the Barrow unit is likely exposed to an annual freeze/thaw cycle, at least above the depth of the 0° seasonal amplitude (approximately 16 m). Furthermore, at the Barrow permafrost tunnel location, Meyer et al. (2010) measure water conductivity values of approximately 7.50 mS/cm at 4–4.5 m in depth and approximately 120 mS/cm (approximately 2.5 times the seawater salinity) in a brine layer at 7 m in depth (both are vertically separated by an ice-wedge system). Based on light stable isotope composition analysis (among other tests), they suggest that the pore water is of nonmarine origin and is kept

unfrozen likely because of the dissolution of formerly deposited marine salts in a lagoonal or estuarine environment. However, the mechanism leading to the presence of this high salinity is not yet clear (Meyer et al., 2010).

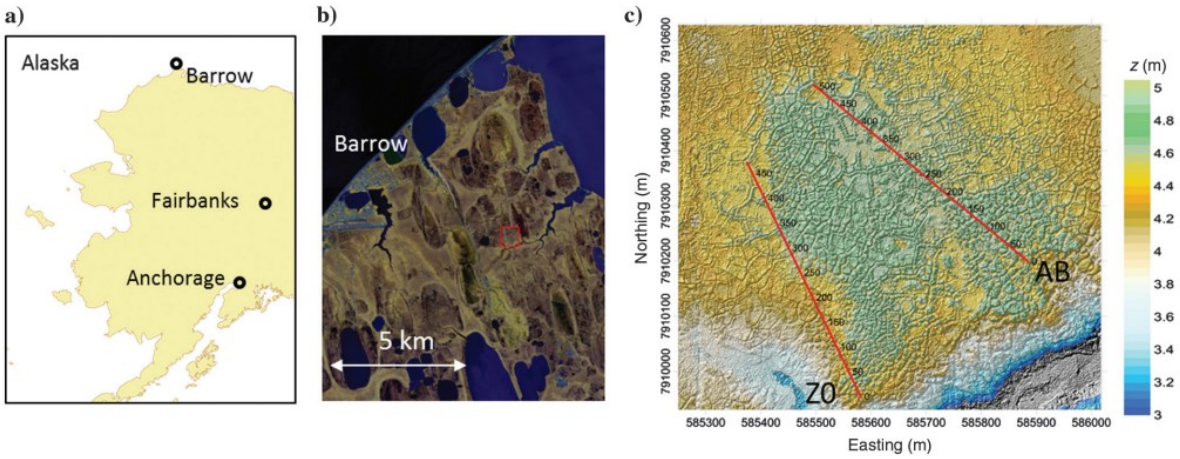

Figure 1. (a) Location of Barrow, Alaska, USA, (b) location of NGEE intensive site near Barrow, and (c) LiDAR-based elevation map showing the location of the ERT transects (from south to north), designated Z0 and AB, at the NGEE Arctic Barrow study site. LiDAR elevation map courtesy of C. Tweedie (University of Texas at El Paso). The low-elevation "gray" region in the southern part of the study site is a channel that drains to the Beaufort Sea.

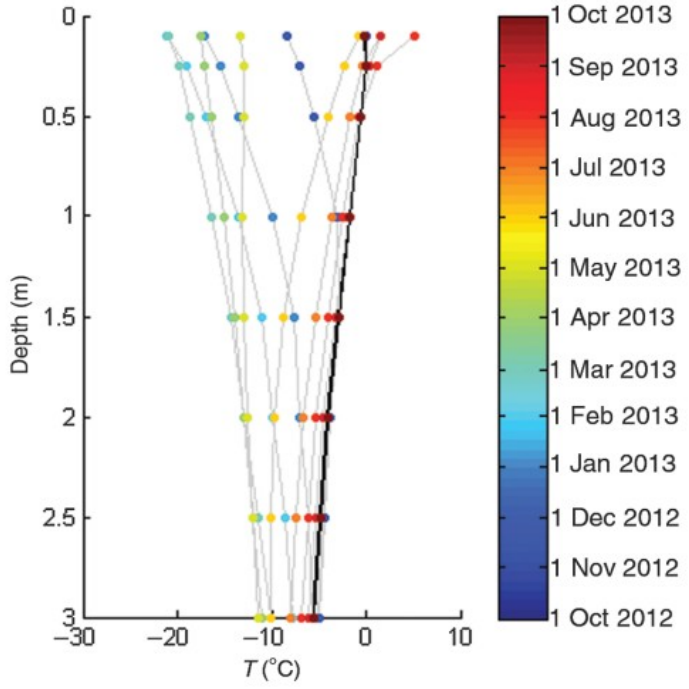

Figure 2. Temperature depth profile at the NGEE site showing the general variations over the year. The two black lines (almost on top of each other) show the temperature on 1 October 2012 and 2013, which are very similar (data courtesy of V. Romanovsky, UAF).

In this study, we perform advanced characterization of the land surface, the top 5 m of permafrost, and their linkages along two approximately 500–m-

long corridors designated Z0 and AB (Figure 1). Geophysical data were collected along the two corridors during various campaigns between 24 September 2011 and 30 May 2013. The Z0 corridor is approximately 475 m long, 20 m wide, and it is oriented in a southeast–northwest direction. The AB footprint is a grid approximately 505 m long, 40 m wide, and it is oriented in a east-southeast–west-northwest direction. ERT transects were acquired along the center of each corridor at the end of the growing season. Concurrently, active-layer thickness measurements and soil samples were collected every 3 m for analysis of activelayer variability along the centerline (Hubbard et al., 2013), and EMI data were collected by foot along both corridors. During a May 2013 campaign, permafrost cores were acquired at some locations along the centerlines, and EMI data were acquired by snowmobile over a larger region that included both corridors.

METHODS AND APPLICATIONS

Permafrost EC and petrophysical relationships

The spatial distribution of soil EC depends on soil properties, such as water content, fluid EC, lithologic properties, clay conductance, and temperature (e.g., Archie, 1945; Revil et al., 1998; Friedman, 2005). Here, we use a modified Archie's law to describe the relationship at a given temperature T between the bulk conductivity σ_{bT}, fluid conductivity σ_{wT}, and water content W_T as follows:

$$\sigma_{bT} = a\ \sigma_{wT}\ W_T^{mT}, \qquad (1)$$

where mT is defined as the cementation exponent and a is the tortuosity factor. Although a conductivity term is often added on the right side of equation 1 to represent the mineral surface conductance, here we do not include it based on the limited amount of clay present at the investigation site. Similarly, we consider the factor a equal to one, which is often assumed. Although mT is generally defined as a constant between 1.5 and 2 for a specific formation, here we define mT as being influenced by the temperature below the freezing point. This is a reasonable assumption based on the fact that mT represents the soil cementation (and tightness), which can be expected to increase when soil and water freeze. Contrary to the original Archie's law, we directly use the water content W_T by assuming that the saturation is equal to one (or that the exponents of the porosity and saturation terms are equal), which is adequate for our purposes, given the fully or highly saturated soil considered in this study. We refer herein to water content as the soil unfrozen water content, which decreases once soils freeze. The factors that can influence the EC, such as temperature, the exponent mT, the unfrozen water content, and salinity, can be represented through the variables given in the right side of equation 1, and they are described below.

The fluid EC is influenced by the ionic molal conductivity and speciated ion concentration (Visconti et al., 2010; McCleskey et al., 2012) of the ions present in the solute. For field applications in which geochemical information is limited, salinity is generally referred to as total dissolved solid (TDS) in g/l, which is related to fluid conductivity (S/m) at 25°C using $\sigma_{w25} = \mathrm{TDS}/k_e$, where k_e is a correlation factor varying between 0.55 and 0.8. The value of k_e is estimated as being equal to 0.64 for various groundwater samples (Atekwana et al., 2004). In this study, we set k_e equal to 0.71 based on the investigation of saline permafrost soil at the laboratory scale (Y. Wu, personal communication, 2015).

The fluid EC is influenced by changes in temperature and related mechanisms. Temperature influences the fluid viscosity and the mobility of ions, which both influence fluid conductivity (Visconti et al., 2010; McCleskey et al., 2012). For field application, temperature above freezing point and fluid conductivity is often related using a linear model of the form:

$$\sigma_{wT} = \sigma_{wT_0}[1 - \beta(T_0 - T)], \qquad (2)$$

where σ_{wT} is the recorded fluid EC at temperature T, σ_{wT_0} is the fluid EC at the reference temperature T_0, β is the fractional change per degree Celsius and has been defined equal to 0.0183 (Hayley et al., 2007) and 0.0187 (Hayashi, 2004) for samples between 0°C and 25°C and to 0.023 for the range 25°C–200°C (Revil et al., 1998). Here, we use a slope of 0.0187, which translates to a 1.87% increase in water EC per degree Celsius.

Furthermore, once the temperature drops below the freezing point, the resistivity increases until all the water is frozen. In the presence of freshwater and negligible salinity, an exponential relation has been commonly used to relate resistivity to temperature (McGinnis et al., 1973). This representation has led to satisfactory results for loose soils (e.g., Hauck, 2002; Wu et al., 2013), although being inappropriate for low-permeability rocks (e.g., Krautblatter et al., 2010). If salinity is nonnegligible, part of the fluid will freeze into pure ice, whereas the solutes are rejected and migrate into the unfrozen fluid, increasing the salinity of the unfrozen fluid and thus creating a highly saline solute with strong depression of its freezing point (Aksenov et al., 2011). Thus, freezing processes occurring at a specific temperature can influence EC through changes in unfrozen water content, changes in salinity of the solute (e.g., Hivon and Sego, 1995; Nicolsky and Shakhova, 2010), and changes in the lithologic parameters.

One approach that has been used in various studies (e.g., Nicolsky et al., 2012) to calculate the unfrozen water content at a temperature below the freezing point is given by Hivon and Sego (1995), who demonstrate that the fraction of unfrozen water content f_{wT}, which corresponds to the ratio between unfrozen water content W_T at temperature T and the total water

and ice content W_{T_0}, in various types of soil can be modeled with reasonable accuracy using the following equation:

$$f_{wT} = \frac{W_T}{W_{T_0}} = \frac{\frac{S}{p_T S_T}}{\left(\frac{S}{p_T S_T}\right) + \left(\frac{1-\frac{S}{S_T}}{p_{iT}}\right)}, \qquad (3)$$

where S is the initial salinity of the solution before freezing (assumed to be equal to the NaCl solute concentration before freezing), p_{iT} is the density of ice at given temperature, and S_T and p_T are the in situ salinity and the density of brine in equilibrium with ice at a given temperature, respectively. The variables p_T and p_{iT} can be calculated using an empirical relationship (e.g., Maidment, 1993). Hivon and Sego (1995) estimate S_T (and later p_T) using a sodium chloride-water binary phase diagram (Hivon and Sego, 1995) assuming that S_T corresponds to the equilibrium fluid salinity at each temperature. Indeed, the freezing point can be estimated from the molality of NaCl in solution, or vice versa, using the Van't Hoff equation (e.g., Maidment, 1993) or various empirical equations (Potter et al., 1978; Velli and Grishin, 1983; Hall et al., 1988; Bodnar, 1993). All of these equations show fairly similar trends, but the relative difference at a given temperature can be as high as 10%. The equation of Velli and Grishin (1983) determined for soils shows an even larger difference, and we did not find another study to corroborate their results. Here, we used the equation of Potter et al. (1978): It is very similar to that of Bodnar (1993), and it is given as

$$S_T = MM_{\mathrm{NaCl}}(0.30604\,dT - 2.86e{-}3\,dT^2 + 4.87e{-}6\,dT^3), \quad (4)$$

where dT is the freezing-point depression and MM_{NaCl} is the molar mass of NaCl (58.44 g/mol). The corresponding fluid conductivity σ_{wT} is then obtained by considering S_T being equal to TDS and using the correlation factor k_e and the temperature correction in equation 2.

Equation 3 can be further simplified by setting p_T and p_{iT} equal to one, which we believe is acceptable for this study, considering the range of uncertainty in process modeling. By incorporating the conductivity term in the simplified equation 3, we obtain

$$f_{wT} = \frac{W_T}{W_{T_0}} = \frac{\sigma_{wT_0}}{\sigma_{wT}}[1 - \beta(T_0 - T)], \qquad (5)$$

which could be similarly obtained based on a simple conceptual model that the increase in the in situ salinity is proportional to the decrease in the unfrozen water due to salt exclusion during ice formation. Here, σ_{wT_0} is

related to the fluid salinity of the entirely thawed soil (referred to here as initial salinity), and σ_{wT} is related to the salinity of the unfrozen water at temperature T.

For field applications, the porosity (considered equal to the total water and ice content in this study) and the in situ fluid salinity as well as the initial salinity are not available, and thus investigating the controls on the bulk resistivity using field geophysical approaches requires reliance on some prior constraints. In this field study, we will first estimate the unfrozen water content from the bulk conductivity ERT data using equation 1, in which in situ temperature measurements are used to estimate the in situ salinity ST (equation 4) and the temperature-corrected σ_{wT} and to control the exponent mT The exponent mT is linearly varying between 1.8 at −0.5°C and 2.1 at −7.5°C. This choice is relatively arbitrary but pragmatic, given that mT likely decreases along that trend during freezing, whereas it is clear that the uncertainty in the range and slope is most critical when salinity is negligible or when the in situ temperature is close to the freezing point. The estimated unfrozen water content is then used in equation 5 to estimate the initial salinity of the unfrozen soil if the porosity is known, or vice versa. In fact, based on equation 5, it is obvious that soil at a given temperature, with specific unfrozen water content and in situ salinity, can correspond to various soils that have the same product of initial salinity and porosity. This means that if both are unknown, estimation of initial salinity and porosity requires further constraints (discussed further in the section “Comparison of ERT and core-based properties versus depth”). Although it is clear that the model devel opment and simplifications described above may produce substantial estimation error (on the order of 20%–30%), the simplifications are important for interpreting field electric data.

ERT data acquisition and inversion

The ERT transects were acquired along two approximately 500-m transects with a 0.5-m electrode spacing and using a 112-electrode Advanced Geosciences, Inc., SuperSting R8 system, a dipole-dipole survey geometry, and a roll-along acquisition strategy. The centerline transects in the Z0 and AB corridors were acquired in September 2011 and September 2012, respectively. Active layer thickness and EM38 measurements repeated over several years and point measurements (i.e., temperature) indicate that the distribution of activelayer depth, the bulk EC, and temperature distributions are very similar at end of each of these growing seasons (data not shown). Thus, it is reasonable to compare ERT data collected at the end of the growing season in two subsequent years. For both ERT transects, the largest distance between the closest injection and potential electrode was 18 m, whereas the largest distance between the two injection (or potential) electrodes was 3 m. In addition to the two long transects, a smaller high-resolution pseudo-3D grid of multiple ERT profiles was acquired using a Multi-Phase Technologies DAS-1 system during the September 2012 campaign. The grid is located between 67.5 and 79.5 m along the AB transect, and it

consists of nine parallel lines perpendicularly crossing the AB transect. Each line is 27.5 m long with 0.5 m electrode spacing.

Low-quality ERT measurements were removed from all data sets, including signals associated with measured potentials less than 3 mV. The electrode locations and elevations were adjusted based on real-time kinematic global positioning system (RTK differential GPS) measurements. All the data were inverted for electric resistivity using CRTomo, which is a smoothness-constraint inversion code that is based on a finite-element algorithm and that solves for resistivity within a 2D region of interest (Kemna, 2000). The obtained mean absolute difference between the calculated and measured data was approximately 10%. The ERT transect along Z0 is published by Hubbard et al. (2013), whereas no permafrost core data analysis and soil properties estimation had been done at that time.

Frequency-domain EMI data acquisition

In this study, the EMI data were collected with an EM38-MK2 (McNeill, 1980; Geonics, 2009) operating at a frequency of 14,500 Hz and including two different transmitter-receiver coil separations (1 and 0.5 m). Acquisition was performed using an external control unit that allowed for synchronization of the acquisition with positioning from the GPS navigation system. The acquisition, performed over snow-covered ground in May 2012, was performed using vertical coil orientation modes, with the instrument located approximately 0.1 m above the ground surface and positioned in a sled behind a snowmobile to cover a significant part of the NGEE intensive site. Acquisition of EMI data in the Z0 corridor in September 2011 was performed by foot twice, using the vertical and horizontal coil orientation modes, with the instrument located approximately 0.1 and 0.05 m above the ground surface, respectively, and along fourteen 475-m-long transects parallel to the centerline and located 1.5 m from each other (Figure 1). Acquisition of EMI data in the AB corridor in September 2012 was performed by foot, using only the vertical coil orientation modes, with the instrument located approximately 0.1 m above the ground surface, and along fifteen 500-m-long transects parallel to the centerline and located 2 m from each other (Figure 1). To investigate the apparent EC in the region near the two corridors, acquisition of EMI data was also acquired elsewhere along approximately 500-m transects using the same configuration.

Standard tool adjustments were performed using the instrument protocol (Geonics, 2009). Initial processing of the data consisted of correcting the data to obtain the mean values inferred from multiple adjustments at a specific location (required a shift < 1 mS/m) to limit adjustment uncertainty. Data acquired along the Z0 transect in September 2011 were used to develop a novel multiparameter grid-search-based approach to estimate the distribution of EC in the active layer with an uncertainty framework (Dafflon et al., 2013). Results showed that the EMI estimated mode of the top-layer (thawed layer) EC distribution was consistent with the results obtained using

ERT. In this study, we consider all the data acquired during the various campaigns (with frozen and unfrozen active layer) to image the EC variations over the intensive site at two different times of the year — in September and May. We did not perform inversion of all these data sets because, besides the data collected in September 2011, only the 1-m coil separation in the vertical direction provided highly consistent data sets without significant drift during acquisition.

3D landscape imaging using low-altitude airborne data

For this study, a kite-based aerial system (Smith et al., 2009; Bryson et al., 2013) was used to lift a consumer-grade digital camera (Sony NEX-5R) above the ground surface. The camera was mounted downward-looking on a Picavet rig attached to the kite line (10 m away from the kite and approximately 2 m below the kite line) to optimize the downward-looking camera stability. The kite-based survey involved automatic acquisition of a picture every 3 s, with the rig located approximately 45 m above the ground and walking along the corridor (return way). From this altitude and with this camera, a downward-looking picture covers a footprint of approximately 73 × 48 m with a pixel size of approximately 0.015 m. The acquisition of sufficient images of the zone of interest with various perspectives was ensured by slight movement of the camera platform. From the large number of images acquired, approximately 70 pictures per corridor were selected manually with privileging various perspectives, no-blur images, relatively downward-looking images, sufficient overlapping, and limiting the number of images to limit computing time. The surveyed corridors were equipped with a network of ground control points made of 24-cm-side white targets, located every 20 m in the targeted 520 × 40 m AB corridor and 480 × 20 m Z0 corridor. The targets were surveyed with a high-precision centimeter-grade RTK differential GPS system.

A DSM and an RGB map were generated using a commercial computer vision software package (PhotoScan from Agisoft LLC) already used successfully in numerous studies (e.g., Dandois and Ellis, 2013). Based on a structure-from-motion approach, this software enables automated feature extraction, bundle adjustment, 3D point cloud generation, and georeferenced map extraction. The software can incorporate information on camera calibration parameters, camera position, and ground control points, to improve the accuracy of the reconstructed DEM and orthomosaics. Although we used ground control points exclusively for this study, the obtained spatial resolution is approximately 0.03 m, and the uncertainty in positioning is smaller than 6 cm in all three dimensions (x; y; z).

Core analysis

Core data provide important information about the physical properties of the permafrost, and they also provide ground-truthing for geophysical interpretation. Cores were acquired at various locations along the Z0 and AB transects. Core data include core AB#136 (meaning at 136 m from the

southernmost end of the AB transect), core AB#159, core AB#446, core Z0#305 (meaning at 305 m from the southernmost end of the Z0 transect), and core Z0#146. Cores Z0#146 and AB#136 were collected with a 7.62-cm-diameter SIPRE soil corer using hydraulic advancing (using a Big Beaver drill rig) and a tripod (using an earthquake auger), respectively. Cores AB#446, AB#159, and Z0#305 were collected with a 5.08-cm-diameter soil corer using a Russian power auger. Typical core depths ranged from 1.5 to 4 m below the ground surface. Retrieved cores were kept frozen until analysis. X-ray computed tomography (CT) scanning was initially performed on all cores, and the resulting images were used to guide the core sectioning and image wet bulk density. CT scanning was performed using a modified medical General Electric LightSpeed 16 CT scanner. Extracted core samples of all cores except AB#136 ranged from 1.25 to 4 cm thick, whereas sample thicknesses for core AB#136 ranged from 6 to 8 cm thick.

Core measurements for each sample consisted of volume measurements, bulk density, ice content, and organic matter content. Volume measurements were performed using two different methods: (1) physical measurement of the sample thickness and diameter (all) and (2) the bag method (only for core AB#136). The bag method (Archimedes' principle) uses a thin-walled plastic bag that is vacuum sealed after the sample is placed inside the bag. After submerging the sample and bag in a large beaker of water (chilled to 1°C to prevent the sample from melting), set upon a scale that was initially zeroed (with the empty bag in it), the volume of the displaced water (the volume of the sample) is obtained by the change in weight. This method of volume measurement proved to be more accurate than physically measuring the sample thickness and diameter of samples that cannot be cut uniformly even. A side-by-side comparison done when processing core AB#136 (as well as a comparison with the CT scans' inferred bulk density) proved that the bulk density and ice content measured earlier in cores AB#159, AB#446, and Z0#305 were related to larger uncertainty than for core AB#136 because of their small sample thickness and the approach used to measure their volume.

After the volume and weight of the soil samples (frozen state) were measured, samples were thawed to collect pore water for fluid conductivity measurement. Following fluid extraction, samples were placed into a 65°C oven to dry for 24 h and reweighed, and then they were placed in the oven for an additional 24 h for a final weighing to ensure that complete drying was achieved. Then, the loss-on-ignition approach (Dean, 1974) was conducted to estimate the organic matter content in the dry sample (mass/mass concentration) by taking a fractional portion of the original sample initially weighed, placing that portion into a 500°C oven for 8 h, and then reweighing. The process was repeated until no significant change in weight was detected. The wet bulk density was obtained from the volume and weight of the frozen samples. The dry bulk density was obtained similarly but with the weight of the dry samples. The ice content was calculated using the volume

of the frozen sample and the difference between the frozen and dry weight of the sample with correction for the ice density. The organic matter content in the dry sample was then used with the dry bulk density to estimate the organic matter content in the soil (mass/volume concentration).

RESULTS AND DISCUSSION

Large-scale trends in electric conductivity

We first examine the spatially extensive apparent EC measurements that were obtained using the EMI approach during a campaign at the end of the growing season (Figure 3a). The growing-season EMI data reveal lower EC values on the northern part of the intensive site. This lower EC signature was surprising, given the observation of standing surface water (up to 0.5 m deep) in many ponds and troughs and that previous studies had documented a generally thicker thaw layer and wetter soil on the northern part of the study area (e.g., Hubbard et al., 2013). In addition, a “frozen/winter” EMI data set was collected in this region during May 2012, during a time when the active layer was completely frozen and snow covered the ground (Figure 3b). The frozen season data set reveals very similar trends compared with the growing season data set, although (as expected) all the measured EC values are smaller. These results indicate that large-scale variations in EMI-obtained EC measurements over the site are largely controlled by variability in the permafrost ice and water content and salinity. The higher apparent EC values at the end of the growing season (compared with the end of the winter) are attributed to the variability in thaw layer properties (increased thickness and water content) and the larger fraction of unfrozen water content in saline permafrost during that time. Comparison between the EC and the trend in topography and its gradient (shown by pink to purple isolines in Figure 3) shows that the lowest apparent conductivity values tend to be located in the flattest area (northern part), in which the water is drained less efficiently and where a majority of LCPs are present. Highest apparent conductivity values are located close to a channel that drains water toward the ocean, whereas some relatively low conductivity spots are located at the highest elevations of the site (e.g., the dark purple isoline along the AB transect).

Because only one configuration has been successfully acquired over the entire site, EMI data inversion cannot be performed over the entire site. More advanced interpretation of the EMI measurements relies on the inversion of data collected in October 2011, along the Z0 profile (collocated to the ERT transect), in which sufficiently different configurations have been successfully acquired (Dafflon et al., 2013). Results have shown that inverted EM data enable reliable estimation of active-layer bulk conductivity and confirm the presence of the saline layer along the profile while located deeper on the north side than on the south side (Dafflon et al., 2013). However, the EM data cannot provide precise depth estimation for the top of

the saline layer without additional constraints because of the significant nonuniqueness present in such a data set.

Electric resistance tomography

In contrast to the spatially extensive yet low-resolution EMI results discussed above, the ERT 3D grid (Figure 4) provides an extremely high resolution image of the EC distribution below a single FCP (raised high). The shallowest bulk EC distribution reveals the significant control of the microtopography on the surface-water and active-layer moisture, which influences the bulk EC response. Below the thawed layer, the bulk resistivity distribution distinguishes the presence of ice wedges (shown by very high resistivity values) below the wide trough and below small troughs or cracks. Their presence can be distinguished from the surrounding, less resistive frozen soil, and the conductive material underneath. Although sharp boundaries between these various zones cannot be identified because of inversion smoothing, the change in resistivity values between these various zones is large (one to two orders of magnitude) over a small spatial scale (0.5–1 m), and thus the uncertainty related to the transition zone is relatively limited.

The more spatially extensive 2D ERT data sets collected along the Z0 and AB transects permit investigation of permafrost characterization beneath a range of polygon types and their comparison to the kite-based DSM and color mosaic. Figure 5 shows the approximately 500-m-long ERT along the Z0 and AB transects, and the corresponding DSM and mosaic obtained from kite-based aerial imaging, covering approximately 500 × 40 m corridor with the ERT transect along the centerline. Similar to the ERT 3D grid, the 2D ERT transects reveal low-resistivity values in the thawed layer (ranging from approximately 30 to 400 ohm-m) overlying a more resistive zone that indicates frozen ground with variable soil properties, and a deeper low-resistivity zone due to the presence of saline permafrost. Figure 5 also shows that the resistive frozen ground has a generally strong variability, along the Z0 and AB transects, with values between 400 and 30,000 ohm-m. Consistent with the EMI responses (Figure 3), high-resistivity regions are generally localized on the north end of the transects. More localized high-resistivity (tooth-shaped) features are interpreted to be ice wedges or other ice-rich structures. These high-resistivity structures are located generally below troughs (indicated by the gray intervals on the color mosaic in Figure 5) and cracks, in which ice wedges are expected. This suggests that ERT can be useful for identifying the presence of ice-rich structures and possibly for investigating theories associated with ice-wedge polygon formation and evolution. However, as is further discussed below, the relationship is not unique, as illustrated by some high-resistivity features observed below the center of some LCP and FCP polygons.

Figure 5 also shows that low-resistivity values are present in the deepest part of a portion of the ERT profiles, with values ranging from 40 to less than 4 ohm-m. Along Z0, low-resistivity values are more pronounced and

shallower in the interval between a distance of 80 and 260 m along the profile, which corresponds to the lowest topographic elevations along the profile and is located on the edge of a channel draining water toward the ocean. Along the AB transect, these low-resistivity values are more pronounced and shallower in the interval a distance of between 150 and 160 m, which corresponds to the highest topography elevations at the NGEE site. Thus, the low-resistivity permafrost zone is not only exclusively related to surface elevation, marine incursion, or sediment origin, but also to ice segregation and solute migration. It is also notable that the edges of the channel system (coincident with the low-resistivity region on Z0) and the high-elevation point (coincident with the low-resistivity region on AB) likely have higher drainage efficiency than does the LCP region (coincident with the high-resistivity region on AB). The trends in the ERT profiles along AB and Z0 transect are very consistent with the EMI data (Figures 3 and 5). In addition, although not shown here, the ERT data show a strong decrease in resistivity at some particular depth everywhere along the profiles, which indicates that the saline layer is present everywhere, although at varying depths.

Covariation of permafrost and geomorphic features

Based on the high-resolution color mosaic and DSM, all troughs and cracks larger than 0.4 m were semiautomatically picked along the Z0 and AB centerlines; the picked intervals are shown in gray on the color mosaic, DSM, and along the ERT transect (Figure 5). An automatic simple detection approach was used to identify and delineate zones with resistivity larger than 950 ohm-m below the trough intervals. The delineated zones are shown by the blue contour lines in the ERT profiles within Figure 5a and 5d. The 950 ohm-m value was determined based on the presence of a minimum in a binomialshaped resistivity frequency distribution, and enabled an ice-wedge vertical delineation consistent with the one observed at the Z0#146 core location (discussed in the section “Comparison of ERT and core-based properties versus depth”).

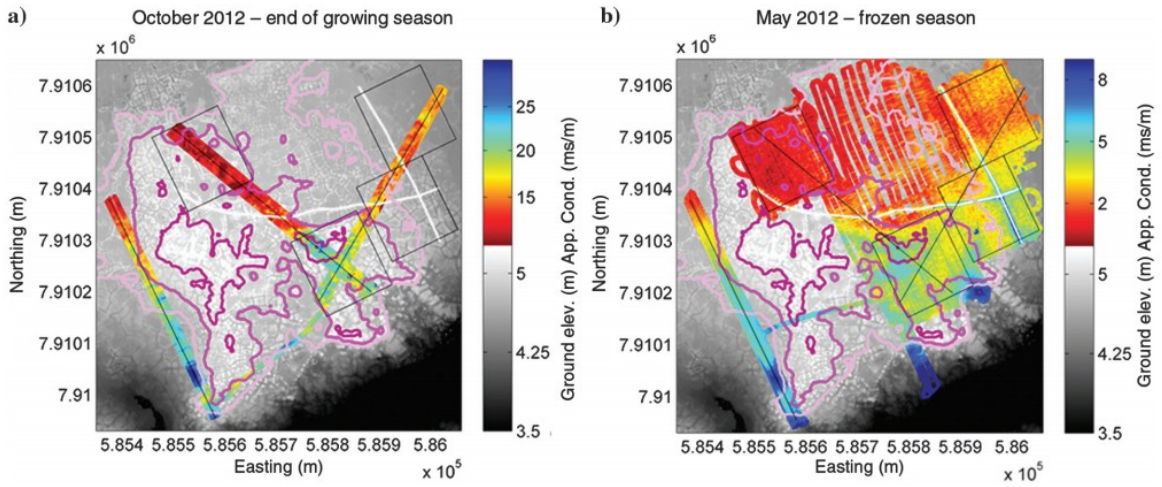

Figure 3. Apparent conductivity (mS/m) from EMI (EM38 1 m, 14.5 kHz) surveys performed in (a) October 2012 and (b) May 2012. Various isolines (from the smoothed LiDAR image) are shown by the pink to purple lines. The apparent conductivity variations observed in October (all being higher than in May) are attributed to moisture content variations in the active layer superposed with the influence of a deep conductive layer that is also visible in May. The black lines indicate location of various investigation sites, and the white lines show location of power lines on the ground.

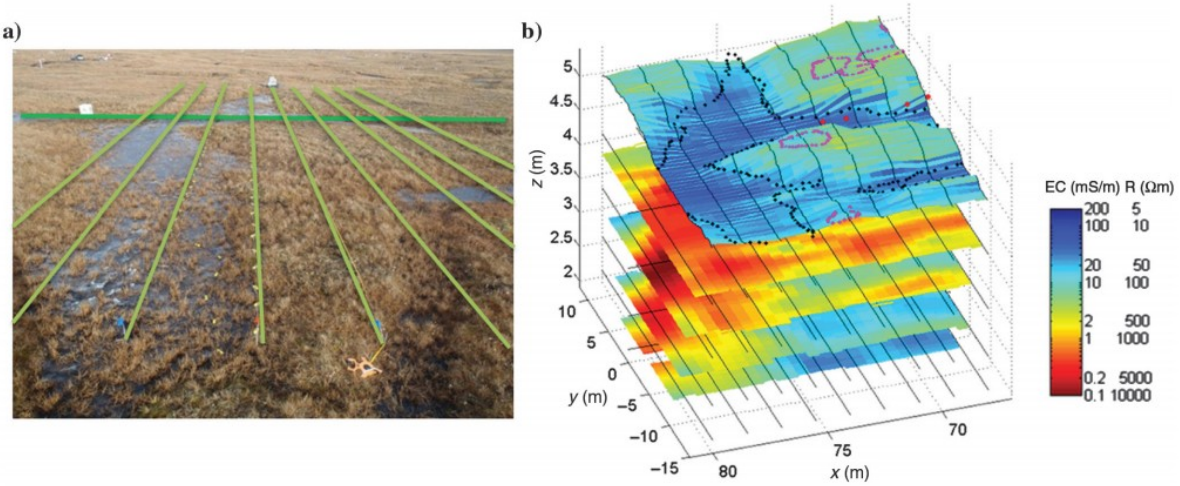

Figure 4. (a) Locations of nine 27.5-m-long 2D resistivity profiles (green lines), which are oriented perpendicular to the AB transect (dark green) between AB stations 67.5 and 79.5 m and (b) 3D reconstruction of electric conductivity distribution from the multiple 2D inverted resistivity profiles (black lines). The edges of the surface water are shown with the black dots on the top slice shaped by the topographic elevation. The purple dots indicate the location of isolated small nonsorted circles. The low EC values indicate ice-wedges located mainly below the troughs. The high-conductivity values indicate the surface water and the deeper saline layer.

Results show that troughs and cracks visible on the color mosaic are always correlated with high-resistivity localized features in the ERT. However, two very different situations prevail. In many regions, these features are limited to the troughs' lateral extent and thus are interpreted to be ice wedges, such as along the Z0 profile and between 0 and 290 m along the AB profile. In this type of environment, ice wedges can be clearly identified by ERT. Note that in HCP zones between 0 and 90 m, the density of the troughs and cracks is very high (likely more than picked on the mosaic and corresponding to different ice-wedge generations and numerous ice veins) and the lower resolution ERT cannot distinguish various ice wedges from each other. In other regions (such as after 250 m along Z0 and after 200 m along AB), ice

wedges are close to very resistive zones below the center of the polygons. In some cases, the approach was not able to automatically delineate icewedge zones; an example is illustrated along the AB transect between 290 and 500 m (the blue dashed lines in Figure 5d). Although LCPs in this region look similar to those encountered along the Z0 transect and are expected to have ice wedges below the troughs, icewedge detection with ERT was not successful because of the limited contrast in resistivity between ice wedges and the surrounding permafrost at this location.

We used the ERT and DSM data sets to estimate characteristics of and relationships between ice wedges and polygon troughs. Given that the Z0 and AB transects traverse polygons at random orientations, we expect that the average density of troughs and ice wedges along the various polygon intervals is representative of the general characteristics of each polygon type (e.g., HCP, FCP, and LCP). Along the Z0 transect, troughs and ice-wedge lateral extents cover 47% and 75% of the HCP interval, respectively. Troughs and icewedge lateral extents cover each 17% of the FCP interval along Z0, they cover 29% and 46%, respectively, of the FCP interval along the AB transect. Troughs and ice wedges cover only 18% and 19% along the LCP interval in Z0. Although the troughs and ice-wedge lateral extents are not equal, they show a similar trend over the various types of polygons. The highest discrepancies between trough and ice-wedge lateral extents were associated with small-diameter polygons (such as in the HCP interval along the Z0 interval and the FCP interval along AB transect), in which the real ice-wedge density likely falls between both estimates, given that in such a zone, the picked trough intervals likely underestimate the lateral extent of ice wedges whereas the ERT method cannot distinguish ice wedges close to each other.

The above results are consistent with the equation used by Kanevskiy et al. (2013) to relate the ice-wedge content in permafrost to the length of a square polygon block side and to a trough’s lateral extent. Their equation shows that wedge ice volume in permafrost increases exponentially with a decreasing polygon size and an increasing trough width. For example, a polygon with a block side length of 5 m (including the trough) and a trough width of 3 m corresponds to a wedge ice content of 48%, whereas a polygon with a block side length of 15 m or more and a trough width of 3 m or less corresponds to wedge ice content of 19% or less. The above values are based on a volume calculation by representing the wedges as isosceles triangles, and thus they can be expected to be slightly lower than the maximal lateral extent calculated from the ERT profiles. Indeed, these values agree well with the ERT-derived values obtained here, in which HCPs have the smallest average diameters but the widest troughs, where the LCPs have the largest average diameters but fairly small troughs, and where FCPs contain a range of polygons and trough sizes.

We compared the ERT and mosaic data to assess the spatial distribution and characteristics of ice wedges relative to microtopographic features. First,

shapes identified from ERT (the blue lines in Figure 5a and 5d) show a good and positive correlation (correlation coefficient $r = 0.72$; Figure 6a) between maximum lateral and vertical extents of ice-wedge polygons, although we recognize that the regularization involved in ERT inversion may slightly influence such correlations. Interestingly, the inferred relationships show that ice wedges tend to have larger lateral than vertical extent, which is different from observation of exposed ice wedges in several studies (Mackay, 2000; Kokelj et al., 2014). Still, core Z0#146 showed an ice-wedge vertical extent of only 1.7 m for a trough lateral extent of approximately 3 m and thus indicate that although ERT and cores may not capture the bottom tail of the ice wedge (which represents a small volume), the ice-wedge shape may be very field-site dependent and highly variable. Furthermore, the weaker relationship between the lateral extent of the trough and vertical extent of ice wedge ($r = 0.39$; Figure 6b) shows that the size of the trough is not the only parameter controlling the vertical extent of an ice wedge. These results demonstrate the complexity of the subsurface and the difficulty in predicting precisely the distribution of subsurface features from DSM and mosaic, although rough estimates of ice-wedge distribution can be inferred. Using more metrics to characterize the shape of a trough may improve the relationship.

Comparison of ERT and core-based properties versus depth

Results from the AB#136 and AB#159 cores, both located in a zone with low-resistivity permafrost along the AB profile, show that the fluid conductivity measured from the cores generally correlates with in situ bulk EC depth trends measured using ERT. The fluid conductivity values measured from AB#136 samples (Figure 7a) are 1.4 mS/cm at 0.45 m depth, and 5.1 mS/cm (approximately 3.6 g/l TDS or 10% of seawater salinity) at a 0.75-m depth, and they tend to increase with depth, with the highest value of 30 mS/cm at 3.55-m depth. Salinity measurements at AB#159 show similar trends, with fluid conductivity equal to 2.8 mS/cm at 0.77-m depth, and they tend to increase with depth, with the highest values of 15.4 mS/m at 1.68-m depth. In addition, the bottom part of core AB#159 between 2.6 and 3 m, which was used in a laboratory experiment, showed a fluid conductivity equal to 62.3 mS/cm and a salinity equal to 45 g/l. Due to salt exclusion during ice formation, we expect the unfrozen water’s in situ salinity to be much higher than the above fluid conductivity values, which were measured from water extracted from the core samples after they thawed.

Another important characteristic of AB#136 core data is that the increase in salinity with depth is correlated with a decrease in porosity (Figure 8e) and in turn an increase in wet bulk density. Such a negative correlation between the initial salinity and ice content is consistent with the expectation of more limited ice segregation in zones in which unfrozen saline water migrated or became concentrated. The AB#159 core data (Figure 7b) confirm these observations, although the approach used to measure the volume of the sample contributes to larger uncertainty in estimated porosity. In addition,

AB#159 samples show that variations over a small spatial scale cannot be perfectly captured by ERT, as expected due to the different measurement support scales and resolutions. An additional interesting behavior of the saline layer sampled at AB#136 is the relatively high organic matter content in a given volume of soil, which is not obvious when looking at the mass/mass concentration of organic matter in dry soil only and which is partly due to the lower porosity of the saline layer. This finding, and the differences between mass/mass and mass/volume organic matter content in general, indicates the importance of estimating soil porosity to investigate soil organic matter content distribution.

Core sample measurements from AB#136 and AB#159 indicate how salinity and ice/water content contribute to the general decrease in bulk resistivity with depth along a large part of the ERT transect. In addition, the core measurements explain why ice wedges composed of relatively fresh water are easily identifiable as a high-resistivity response. Core Z0#146 was drilled in a trough to verify the presence and size of such an ice wedge identified in the ERT transect. The bottom of the ice wedge was reached at 1.7 m, similar to the ERT estimated depth of 1.6 m obtained using a boundary value of 950 ohm-m. In fact, changing this boundary value does not significantly influence the estimate because of the very strong gradient between the ice wedge and the underlying conductive layer (Figure 7). The only processed sample at this location was located 0.1 m below the bottom of the ice wedge and had a fluid conductivity equal to 15 mS/cm, which again confirmed results from the AB#136 and AB#159 samples.

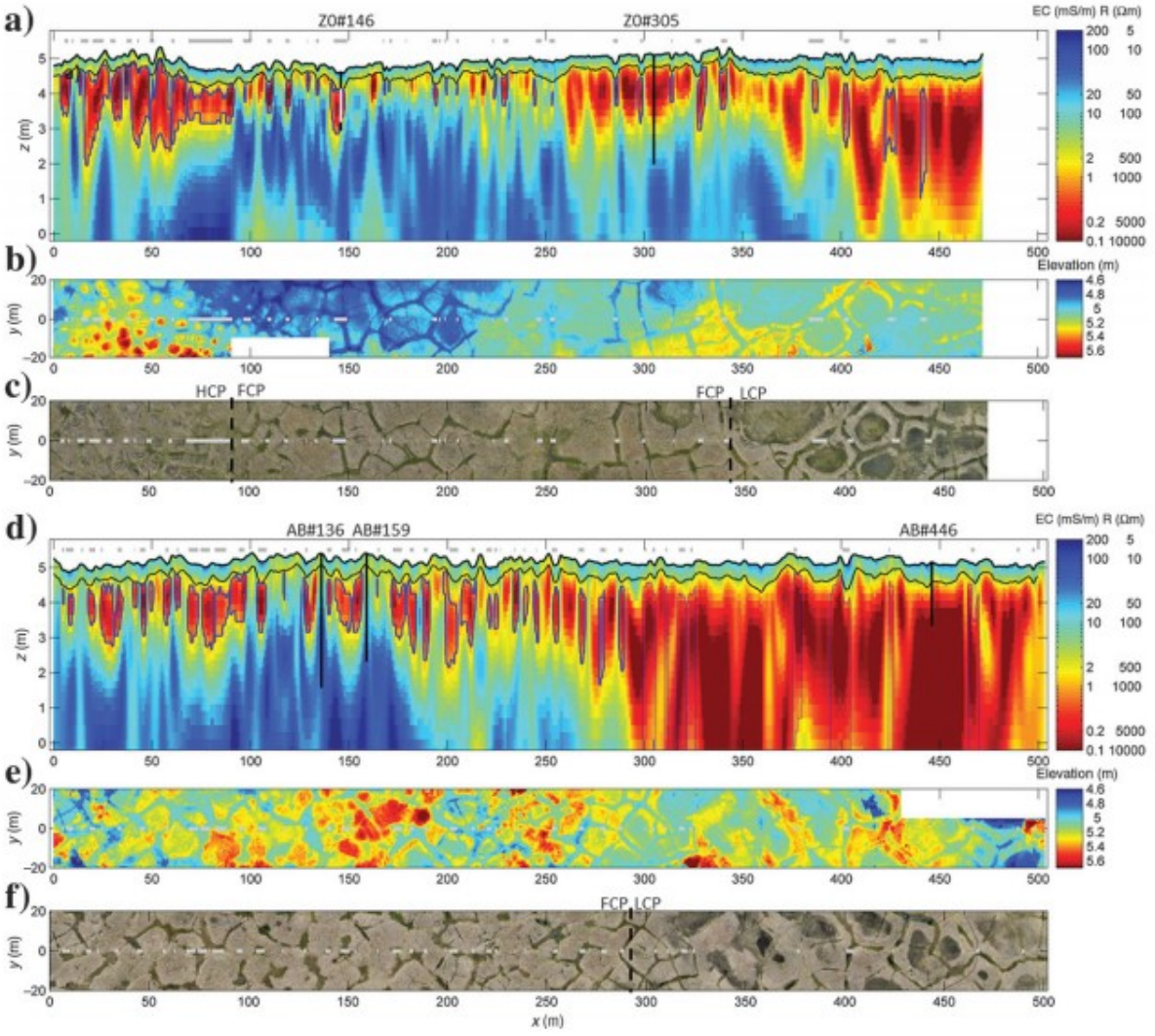

Figure 5. (a) ERT along the Z0 transect (the black line indicates the probe-measured base of the active layer), (b) DSM (elevation [m]), and (c) mosaic along the 470- × 40- m corridor (including the Z0 transect) obtained from kite-based aerial imaging. The ERT transect has been acquired along the Z0 corridor centerline ($Y = 0$ m) in (b and c), in which the gray lines indicate the trough locations. The blue contour lines surrounding the very resistive zones in (a) show autonomously delineated ice wedges, whereas the dashed blue contour lines indicate locations with expected but not delineated ice-wedges. (d-f) The same descriptions as (a-c) but along the AB transect.

Results from cores AB#446 and Z0#305, both located in a zone of high resistivity between 0 and at least 2-m depth, show very different results (Figure 7). At these locations, the fluid conductivity is very low, and its fluctuation does not significantly influence the electric resistivity. Indeed, in this case, the top of the permafrost, located between a 0.5- and 1.5-m depth at Z0#305, corresponds to a very resistive region involving high ice and low soil organic matter content, whereas the same interval at AB#446 is related

to less resistive permafrost with similar amounts of ice content but much larger amounts of soil organic matter. In fact, the larger amount of soil organic matter in AB#446 between 0.5 and 1.5 m likely contribute to the lower resistivity response, whereas the proportion of organic-matrix ice in the measured total ice content cannot be estimated. In this regard, the soil organic matter content values measured in this study are in the same range as those measured in other studies around Barrow (e.g., Bockheim et al., 2003). Another interesting aspect of the AB#446 core is that samples and CT scans conducted on core sections deeper than a 1.45-m depth show the presence of a dense, low-ice-content (approximately 0.5), low-fluid-conductivity, sandy soil that is located in the upper part of the most resistive region in the ERT transect along the AB transect. Although we did not succeed in drilling deeper at this location to evaluate the vertical extent of this sandy material, the deeper presence of sandy or gravelly material and/or nonsaturated conditions may explain this high-resistivity response (Figure 7a). Although all the cores did not reach the saline layer, the ERT data suggest that the saline permafrost is present everywhere, whereas it is deeper in the northern part of the corridors.

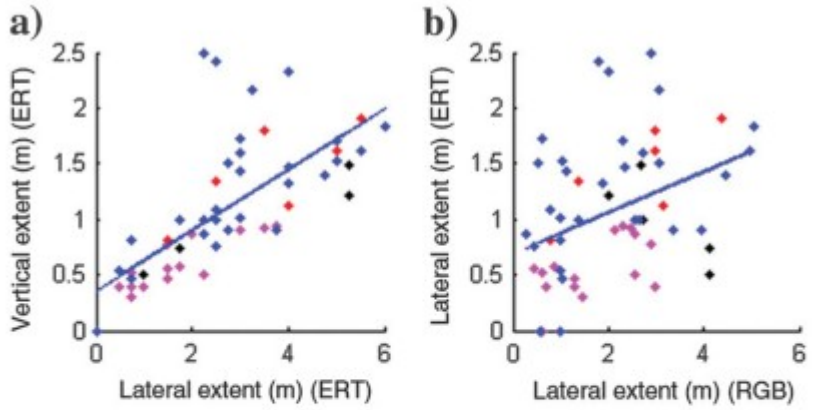

Figure 6. Vertical extent of ice-wedges imaged by ERT versus the lateral extent of (a) ice-wedges imaged by ERT and (b) troughs imaged in the RGB mosaic. The various colors refer to HCP along Z0 (black), FCP along Z0 (pink), LCP along Z0 (red), and FCP along AB (blue). The blue lines show the best-fit linear relationship.

As an ensemble, the core analysis suggests that a change in bulk EC is driven by variations in different soil properties, and that there are several distinct ranges of bulk conductivity (or bulk resistivity R_b [ohm-m]) that reveal distinct sensitivities (Figure 8). The low bulk conductivity range ($0.05 < \sigma_b$[mS/m] < 1.05 or $20{,}000 > R_b$[ohm m] > 950) includes the bulk conductivity values observed for ice wedges and for ice-rich permafrost. In this region, decreasing conductivity is correlated with increasing ice content. This is consistent with results from various studies showing the negative

correlation between the ice content and bulk conductivity (e.g., Fortier et al., 1994). An intermediate conductivity range (1.05 < σ_b[mS/m] < 5 or 950 > R_b[ohm m] > 200) represents the inverse trend whereby an increase in conductivity is observed as the ice content increases. This is plausible when considering the very similar ice content but very different bulk conductivity and soil organic matter content at approximately 1 m in depth in cores AB#305 and AB#446. Indeed, Figure 8f shows that an increase in organic matter content is always correlated with an increase in ice content. This suggests that an increase in organic matter content and organic-matrix ice (which is not distinguished from total ice content) increases conductivity. The second highest conductivity range is a transition range, in which salinity controls the bulk EC and is negatively correlated with porosity (5 < σ_b[mS/m] < 20 or 200 > R_b[ohm m] > 50). In this range, the bulk conductivity increases with decreasing temperature, which means that the temperature itself has a less direct influence on conductivity than do changes in in situ salinity. The upper range of the bulk EC (20 < σ_b[mS/m] or 50 > R_b[ohm m]) is associated with locations where the porosity is the lowest (approximately 0.45 or less) and where fluid conductivity variations alone control changes in bulk EC.

ERT imaging and core analysis provide an opportunity to estimate the spatial distribution of in situ unfrozen water content, porosity, and salinity along the transects. To meet this objective, we estimated the unfrozen water content using equation 1 with ERT-based bulk EC estimates and with in situ salinity estimated using equation 4 with the in situ temperature. Porosity (considered equal to the total water and ice content) and initial salinity values are then investigated using equation 5. Figure 9a shows the relationships between various hypothetical values of bulk conductivity at −5°C, initial salinity, and porosity, and it illustrates that bulk conductivity at a given temperature can correspond to various soils that have the same product of initial salinity and porosity. To estimate the initial salinity and then the porosity (or vice versa) using the field ERT data, we solve equation 5 by considering the relationship observed between the initial fluid EC and porosity from the core samples' analysis (Figure 8e). It is important to keep in mind that this relationship is primarily (and maybe exclusively) adapted for the part of the ERT transects in which salinity is nonnegligible. We use the best-fit linear relationship between the initial salinity and porosity based on all the core samples (Figure 8e), while fixing the minimum porosity at 0.4 (Figure 9a). A minimum porosity is set at 0.4 because we expect that porosity between 0.3 and 0.4 will likely correspond to soil that may contain predominantly porous ice and water (no excess ice) and in which the porosity range is likely to be small relative to the salinity range. Coupling the above relationship with equation 5 enables the estimation of porosity and initial salinity, and it allows for estimation of the related unfrozen water content curve for each bulk conductivity values as shown in Figure 9a (and at −5°C in Figure 9b). Figure 9b confirms that a given change in temperature

has the most significant effect on the resistivity (and unfrozen water content) when it is close to the freezing point and even more so in case of a small freezing-point depression. At lower temperatures (e.g., −5°C), the changes in bulk conductivity due to one-degree variations are much less important. Figure 9 thus illustrates that interpreting the electric conductivity and temperature of permafrost soil close to its thawing point and/or with low initial salinity (under totally unfrozen conditions) infers larger uncertainties.

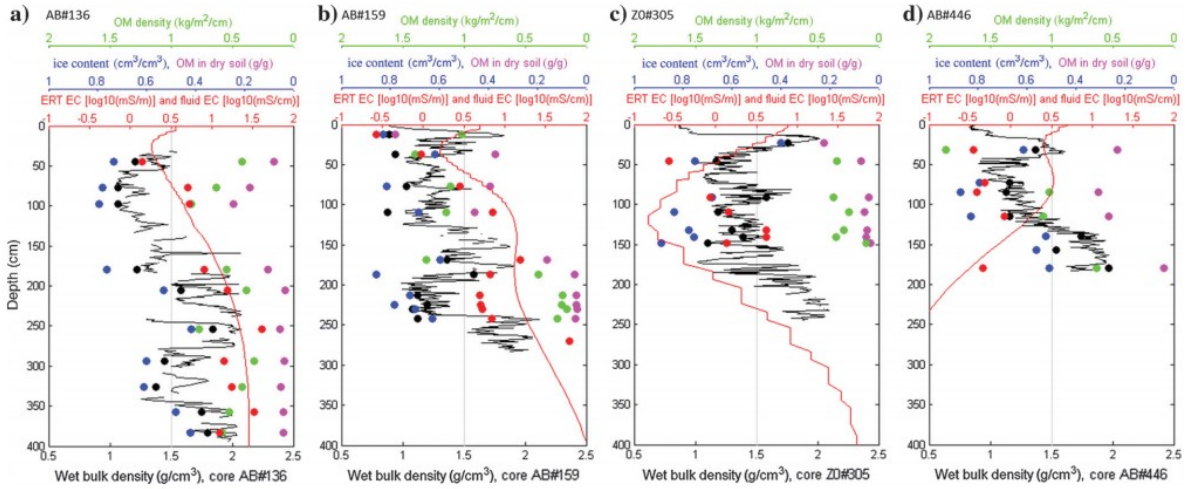

Figure 7. CT scan measured wet bulk density (averaged for each depth) (black line), wet bulk density (black dots), ice content (blue dots), organic matter content in dry soil (mass/mass concentration) (pink dots), organic matter content in soil (mass/volume concentration) (green dots) and fluid conductivity (red dots) from soil samples, and bulk EC from the ERT (red line) at (a) 136 m and (b) 159 m along the AB transect, (c) 305 m along Z0 transect, and (d) 446 m along the AB transect.

We apply the analysis described above to field ERT data sets to estimate the permafrost properties, and we compare the ERT-obtained estimates with collocated core-measured values (Figure 10). To perform this analysis, we make an assumption that the temperature depth profile below a 0.5-m depth (Figure 2) is laterally constant over all the transects. The obtained misfit between the measured and predicted values confirms that we can capture the trend, whereas the precise estimation of values is not possible, especially for low-salinity soil. Considering the difference in the measurement support scale and spatial resolution between ERT and core data, the uncertainty in ERT estimates of conductivity, and the simplifications invoked in the petrophysical model, the results are encouraging.

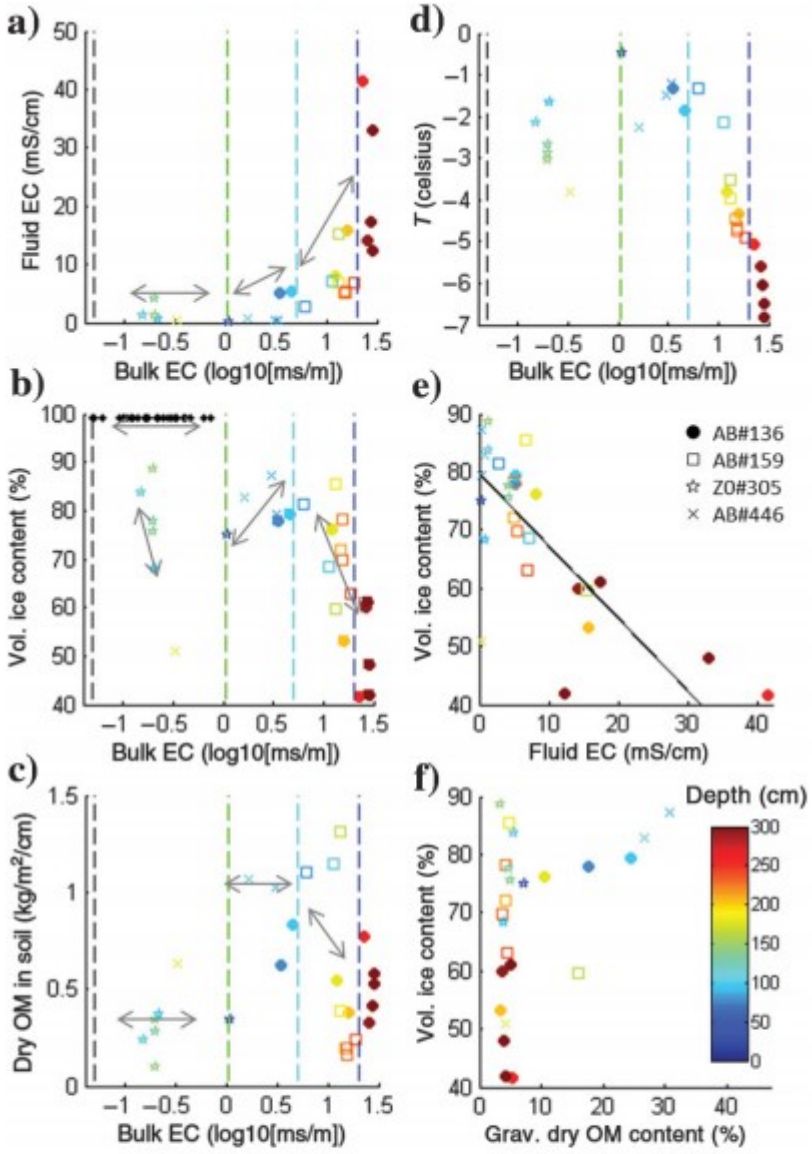

Figure 8. Correlation between soil properties from the core samples and collocated bulk EC from the ERT data at core location AB#136 (filled circle), AB#159 (square), Z0#305 (star), and AB#446 (cross). Bulk EC versus core sample properties including (a) fluid EC, (b) volumetric ice content (black dots show bulk EC from delineated ice-wedges, Figure 5d), (c) organic matter content in soil, and (d) in situ temperature. (e) Fluid EC versus volumetric ice content (the black line shows the best linear fit relationship) and (f) organic matter content in dry soil versus volumetric ice content. The color scale (capped at 300 cm) indicates the depth of the sample, and the vertical dashed lines in panels (a and c) separate different EC behavioral regimes. The various arrows show the different trends in soil properties in the different bulk EC intervals

We extend the method described above to the two ERT transects to estimate the spatial distribution of permafrost properties, including unfrozen water content, initial salinity, and porosity (the volume of water and ice) (Figure 11b–11e and Figure 12b–12e). Although the estimated porosity, initial salinity, and fraction of unfrozen content along the Z0 and AB transect (Figures 11 and 12) may have uncertainty as high as 30% and are less reliable on the northern part of the AB transect, the coupled analysis with core data enables us to differentiate and investigate various characteristics of permafrost along the transects. From 0 to 250 m along Z0, and from 0 to approximately 200 m along AB, the unfrozen water content and salinity increase gradually with depth, starting as shallow as a few tens of centimeters below the bottom of the active layer, which is consistent with the increasing trend in fluid conductivity in cores AB#136 and AB#159 with values between 2.8 and 5.1 mS/cm (approximately 5% and 10% seawater salinity, respectively) at approximately 0.75 m depth. The heterogeneity in porosity, unfrozen water content, and initial salinity is large. In several locations, the soil unfrozen water content increases up to approximately 15% and the fraction of the unfrozen water content in the pores increases up to approximately 35%, with a few locations showing higher values. Finally, the gradual increase in unfrozen water content implies that the freshwater ice wedges can be clearly delineated in these regions. From 250 to 470 m along Z0, and from approximately 200 to 500 m along AB, the soil unfrozen water content is very small, which implies low salinity and high porosity (based on the relationship used between the initial salinity and porosity). However, this is not always the case in this region, and thus the porosity, estimated to be approximately 80%, can correspond in reality to any value between 65% and 95% and even to smaller values in regions that are the most resistive.

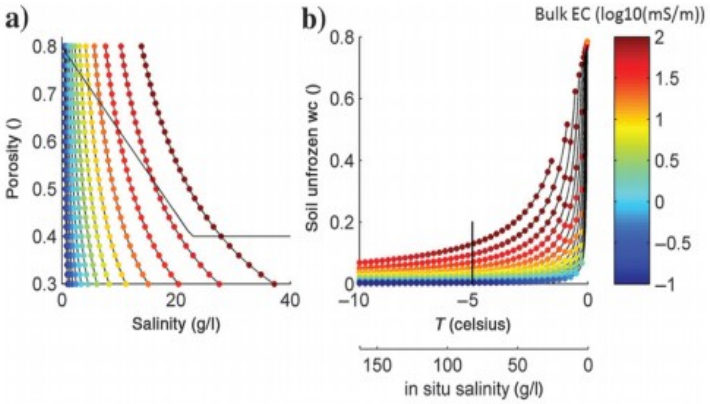

Figure 9. (a) Synthetic example of various pairs of initial salinity (if the soil is thawed) and porosity (considered equal to the total water and ice content) values that correspond to specific bulk electric conductivity values at a given temperature (here 5°C). The black line shows the best-fit linear relationship between samples of porosity and initial salinity for porosity values higher than 0.4 (Figure 8e), whereas porosity is kept equal to 0.4 for higher salinity values. (b) The soil's unfrozen water content predicted at various temperatures (below freezing point) for the pairs of initial salinity and porosity obtained from the bulk electric conductivity and constrained by the relationship shown in (a).

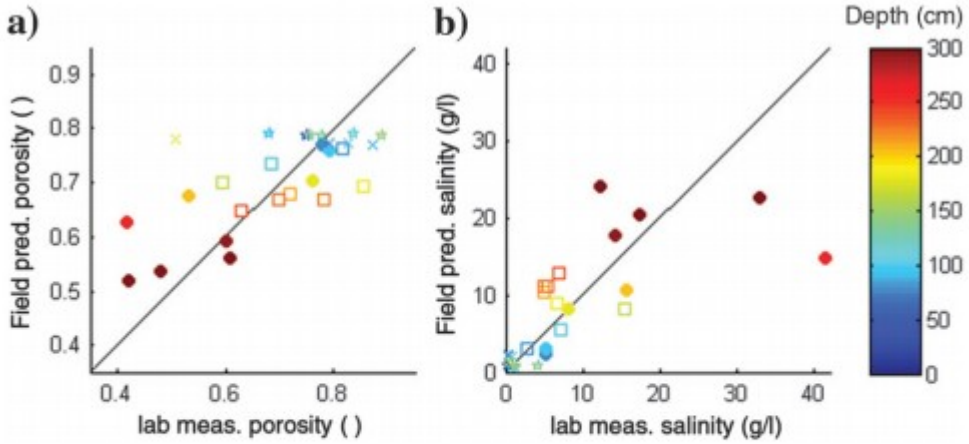

Figure 10. Fit between field (from ERT) and laboratory (from samples) inferred (a) porosity and (b) initial salinity. The markers show the values for cores AB#136 (filled circle), AB#159 (square), Z0#305 (star), and AB#446 (cross).

To delineate the distribution of the main features or characteristics at the site, we make use of the various ranges of electric conductivity defined in Figure 8 to classify the electric conductivity transects into various "behavioral" units after removing ice-wedge detected below troughs (Figures 11f and 12f). In addition to the ranges shown in Figure 8, we included an

additional range corresponding to electric conductivity smaller than 0.05 mS/m (< 20,000 ohm-m) to delineate a very-low-conductivity zone that was not sampled with core and may have different lithologic and cryospheric properties (see the discussion of core AB#446). In addition, the conductivity range corresponding to particularly high organic matter content has been limited to the top 1.2-m depth to avoid misinterpreting the transition from the bottom of the ice wedge into the conductive layer. The results of the feature estimation are shown in Figures 11f and 12f. The results, which are consistent with core sample interpretation and permafrost properties' estimation, emphasize the presence of nonnegligible shallow permafrost salinity on the south side of the two transects and the significant vertical and horizontal variability. Overall, the "rough" soil properties' estimation and classification approach will be useful for parameterizing permafrost models and for guiding field characterization efforts.

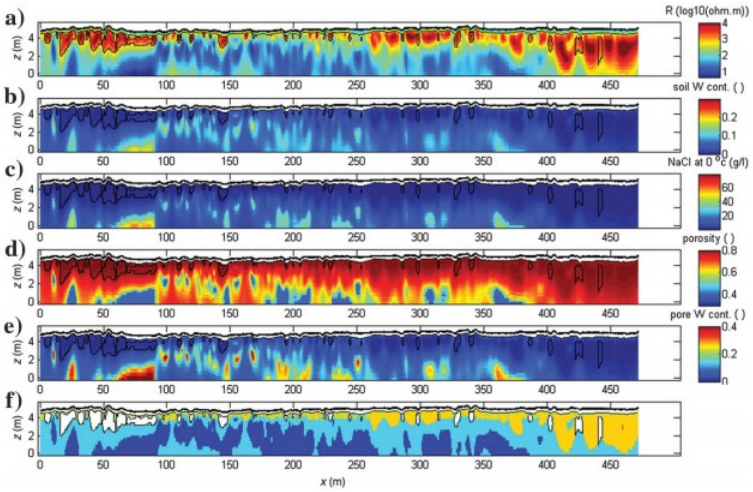

Figure 11. (a) ERT along the Z0 transect (the black line near the ground surface indicates the probe-measured base of the active layer), (b) the estimated permafrost soil unfrozen water content, (c) the estimated initial salinity of the corresponding thawed soil, indicated as the concentration of NaCl, (d) porosity, (e) fraction of unfrozen pore water content, and (f) interpretation of various features (based on Figure 8), including the ice-wedge (white); very ice-rich soil (orange) or possibly sandy/gravelly nonsaturated soil (red); a layer with a likely higher amount of organic matter (green); a layer with increasing salinity with depth, decreasing porosity and variable amount of organic matter (light blue); and a saline layer with limited interstitially segregated ice (dark blue).

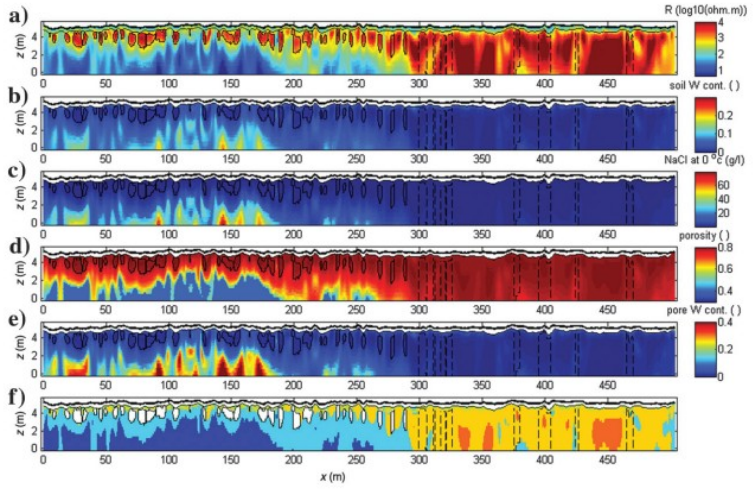

Figure 12. Same as Figure 9 but along the AB transect. Caveat: The petrophysical model characteristics lead to large uncertainties of the estimate in the region between 290 and 500 m, in which salinity does not drive the resistivity variations.

CONCLUSIONS

In this study, we have investigated the shallow ground ice and salinity distribution in a polygon-shaped environment over significant spatial scales

and in a minimally invasive manner. To explore subsurface variability in the top 5-m depth at various scales, we relied on a variety of methods, including ERT, frequency-domain EMI data, and laboratory core analysis. To investigate surface-subsurface covariability, we have inferred digital surface models and color mosaics with low-altitude airborne imaging using a kite-based approach. To evaluate the distribution of various soil properties, we have performed soil analysis on several core samples and we have adapted a petrophysical model.

This study developed and implemented new approaches to provide the first comprehensive examination of permafrost in polygonshaped Arctic tundra using multiple field and lab data sets — data sets that together enable advanced estimation of permafrost properties (including the frozen state, porosity, and salinity) in high resolution with relevant spatial coverage. The results from this study (1) reveal the distribution and characteristics of a relatively continuous but depth-variable shallow, partially unfrozen saline layer with significant salinity observed as shallow as 0.75 m deep at some locations; (2) enable imaging of ice-wedge geometry and estimates of unfrozen water content, total porosity, and salinity at high resolution, providing the first high-resolution glimpse of spatially variable permafrost properties; and (3) document the correlation between topography and permafrost characteristics, including ice wedge and salinity distribution. In particular, this study quantified the presence and nature of nonnegligible saline permafrost, which could be an important factor in ecosystem functioning and civil infrastructure at many other coastal Arctic regions.

This study also provided new insights about permafrost-based petrophysical relationships and field characterization methods. The laboratory analysis led to the documentation of the key controls on electric resistivity in this permafrost region, such as the salinity that is negatively correlated with porosity, the presence of wedge ice, the soil organic matter content, and the lithologic properties. Such analysis is very valuable for applying to feature classification and/or petrophysical models adapted to field geophysical data that in turn enable the understanding of the spatial distribution of the soil properties over a relevant scale. The study also showed the promise of using low-altitude aerial imaging-based reconstruction of DSM and mosaics in conjunction to geophysical data to increase the ability to investigate the surface-subsurface covariability that is important for understanding ecosystem processes and to upscale results at specific sites to a larger spatial extent when possible.

Overall, the results of this paper reveal the utility of field geophysical approaches paired with laboratory analysis to characterize a complex Arctic polygonal landscape, including the spatial distribution of permafrost ice content, salinity, lithologic properties, and organic matter content. The high-resolution data provided unique insights into the covariance between permafrost and land surface properties, two critical compartments in the Arctic ecosystem, and highlights the importance of continued studies to

document the importance of this covariance on ecosystem feedback to climate potentially caused by annual processes (e.g., microbial respiration in the permafrost) and decadal or longer processes (e.g., mass wasting of landscape due to permafrost degradation in cyropeg-rich regions).

ACKNOWLEDGMENTS

The Next-Generation Ecosystem Experiments (NGEE Arctic) project is supported by the Office of Biological and Environmental Research in the DOE Office of Science. This NGEE-Arctic research is supported through contract number DE-AC02- 05CH11231 to Lawrence Berkeley National Laboratory. Data sets are available from Dafflon et al. (2015) or by contacting the authors. Logistical support in Barrow was provided by UMIAQ, LLC. The authors thank S. Wullschleger (NGEE-Arctic PI, ORNL), N. Quinn (LBNL) for lending us EM38 tools, A. Kemna (University of Bonn) for providing 2D complex resistivity imaging codes, C. Tweedie (University of Texas at El Paso) for providing LiDAR data, C. Tweedie and S. Vargas (University of Texas at El Paso) for providing advice in kite-based aerial imaging, A. Kholodov (University of Alaska at Fairbanks) for his help with field coring efforts, V. Romanovsky (University of Alaska at Fairbanks) for providing soil temperature data, and D. Graham (ORNL) for drilling core Z0#146.

REFERENCES

Aksenov, V. I., N. G. Bubnov, G. I. Klinova, A. V. Iospa, and S. G. Gevorkyan, 2011, Water phase transformations in frozen soil under the effect of cryopegs: Water Resources, 38, 934–943, doi: 10.1134/S0097807811070025.

Archie, G. E., 1945, Electrical resistivity log as an aid in determining some reservoir characteristics: Transactions of the American Institute of Mining and Metallurgical Engineers, 146, 322–323, doi: 10.2118/942054-G.

Atekwana, E. A., R. S. Rowe, D. D. Werkema, and F. D. Legall, 2004, The relationship of total dissolved solids measurements to bulk electrical conductivity in an aquifer contaminated with hydrocarbon: Journal of Applied Geophysics, 56, 281–294., doi: 10.1016/S0926-9851(04)00057-6

Berni, J. A. J., P. J. Zarco-Tejada, L. Suarez, and E. Fereres, 2009, Thermal and narrowband multispectral remote sensing for vegetation monitoring from an unmanned aerial vehicle: IEEE Transactions on Geoscience and Remote Sensing, 47, 722–738., doi: 10.1109/TGRS.2008.2010457.

Binley, A., and A. Kemna, 2005, DC resistivity and induced polarization methods, in Y. Rubin, and S. S. Hubbard, eds., Hydrogeophysics: Springer, 129–156.

Black, R. F., 1964, Gubik formation of Quaternary age in northern Alaska: U.S. Geological Survey.

Bockheim, J. G., 2007, Importance of cryoturbation in redistributing organic carbon in permafrost-affected soils: Soil Science Society of America Journal, 71, 1335–1342, doi: 10.2136/sssaj2006.0414N.

Bockheim, J. G., L. R. Everett, K. M. Hinkel, F. E. Nelson, and J. Brown, 1999, Soil organic carbon storage and distribution in Arctic Tundra, Barrow, Alaska: Soil Science Society of America Journal, 63, 934–940, doi: 10.2136/sssaj1999.634934x.

Bockheim, J. G., K. M. Hinkel, and F. E. Nelson, 2003, Predicting carbon storage in tundra soils of arctic Alaska: Soil Science Society of America Journal, 67, 948–950, doi: 10.2136/sssaj2003.0948.

Bodnar, R. J., 1993, Revised equation and table for determining the freezingpoint depression of H2O-NACL solutions: Geochimica et Cosmochimica Acta, 57, 683–684, doi: 10.1016/0016-7037(93)90378-A.

Brouchkov, A., 2002, Nature and distribution of frozen saline sediments on the Russian Arctic coast: Permafrost and Periglacial Processes, 13, 83–90, doi: 10.1002/ppp.411.

Brouchkov, A., 2003, Frozen saline soils of the Arctic coast: Their distribution and engineering properties, in M. Phillips, S. M. Springman, and L. U. Arenson, eds, Permafrost: Lisse, Swets & Zeitlinger, 95–100.

Brown, J., 1969a, Ionic concentration gradient in permafrost, Barrow, Alaska: U.S. Army Cold Regions Research and Engineering Laboratory, Research report.

Brown, J., 1969b, Ionic concentration gradients in permafrost Barrow, Alaska: Cold Regions Research and Engineering Laboratory, U.S. Army Corps of Engineers.

Brown, J., P. C. Miller, L. L. Tieszen, and F. L. Bunnell, 1980, An arctic ecosystem: The coastal tundra at Barrow, Alaska: Dowden, Hutchinson, & Ross.

Brown, J., and P. V. Sellmann, 1973, Permafrost and coastal plain history of arctic Alaska, in M. E. Britton, ed., Alaskan Arctic tundra: The Arctic Institute of North America, 31–47.

Bryson, M., M. Johnson-Roberson, R. J. Murphy, and D. Bongiorno, 2013, Kite aerial photography for low-cost, ultra-high spatial resolution multispectral mapping of intertidal landscapes: Plos ONE, 8, 9, doi: 10.1371/journal.pone.0073550.

Corwin, D. L., and S. M. Lesch, 2005, Characterizing soil spatial variability with apparent soil electrical conductivity: Part II. Case study: Computers and Electronics in Agriculture, 46, 135–152, doi: 10.1016/j.compag.2004 .11.003.

Dafflon, B., S. S. Hubbard, J. E. Peterson, and C. Ulrich, 2015, Electrical resistivity tomography, electromagnetic data, mosaic and DSM, and permafrost cores in Barrow, Alaska: Next Generation Ecosystem Experiments

Arctic Data Collection, Carbon Dioxide Information Analysis Center, Oak Ridge National Laboratory, Data set accessed at, doi: 10 .5440/1233229.

Dafflon, B., S. S. Hubbard, C. Ulrich, and J. E. Peterson, 2013, Electrical conductivity imaging of active layer and permafrost in an Arctic ecosystem, through advanced inversion of electromagnetic induction data: Vadose Zone Journal, 12, no. 4, doi: 10.2136/vzj2012.0161.

Dandois, J. P., and E. C. Ellis, 2013, High spatial resolution three-dimensional mapping of vegetation spectral dynamics using computer vision: Remote Sensing of Environment, 136, 259–276, doi: 10.1016/j.rse .2013.04.005.

Dean, W. E., 1974, Determination of carbonate and organic-matter in calcareous sediments and sedimentary-rocks by loss on ignition — Comparison with other methods: Journal of Sedimentary Petrology, 44, 242–248, doi: 10.1306/74D729D2-2B21-11D7-8648000102C1865D.

Engstrom, R., A. Hope, H. Kwon, D. Stow, and D. Zamolodchikov, 2005, Spatial distribution of near surface soil moisture and its relationship to microtopography in the Alaskan Arctic coastal plain: Nordic Hydrology, 36, 219–234.

Everett, M. E., and M. A. Meju, 2005, Near-surface controlled-source electromagnetic induction: Background and recent advances, in Y. Rubin, and S. S. Hubbard, eds., Hydrogeophysics: Springer, 157–183.

Farquharson, C. G., D. W. Oldenburg, and P. S. Routh, 2003, Simultaneous 1D inversion of loop-loop electromagnetic data for magnetic susceptibility and electrical conductivity: Geophysics, 68, 1857–1869, doi: 10.1190/ 1.1635038.

Fortier, R., M. Allard, and M. K. Seguin, 1994, Effect of physicalproperties of frozen ground on electrical-resistivity logging: Cold Regions Science and Technology, 22, 361–384, doi: 10.1016/0165-232X(94) 90021-3.

Fortier, R., A.-M. LeBlanc, M. Allard, S. Buteau, and F. Calmels, 2008, Internal structure and conditions of permafrost mounds at Umiujaq in Nunavik, Canada, inferred from field investigation and electrical resistivity tomography: Canadian Journal of Earth Sciences, 45, 367–387, doi: 10 .1139/ E08-004.

Friedlingstein, P., P. Cox, R. Betts, Bopp, W. von Bloh, V. Brovkin, P. Cadule, S. Doney, M. Eby, I. Fung, G. Bala, J. John, C. Jones, F. Joos, T. Kato, M. Kawamiya, W. Knorr, K. Lindsay, H. D. Matthews, T. Raddatz, P. Rayner, C. Reick, E. Roeckner, K. G. Schnitzler, R. Schnur, K. Strassmann, A. J. Weaver, C. Yoshikawa, and N. Zeng, 2006, Climate–carbon cycle feedback analysis: Results from the C4MIP model intercomparison: Journal of Climate, 19, 3337–3353, doi: 10.1175/ JCLI3800.1.

Friedman, S. P., 2005, Soil properties influencing apparent electrical conductivity: A review: Computers and Electronics in Agriculture, 46, 45–70, doi: 10.1016/j.compag.2004.11.001.

Geonics, 2009, EM38-MK2 Ground conductivity meter operating manual.

Gilichinsky, D., E. Rivkina, C. Bakermans, V. Shcherbakova, L. Petrovskaya, S. Ozerskaya, N. Ivanushkina, G. Kochkina, K. Laurinavichuis, S. Pecheritsina, R. Fattakhova, and J. M. Tiedje, 2005, Biodiversity of cryopegs in permafrost: FEMS Microbiology Ecology, 53, 117–128, doi: 10.1016/j.femsec.2005.02.003.

Goswami, S., J. A. Gamon, and C. E. Tweedie, 2011, Surface hydrology of an arctic ecosystem: Multiscale analysis of a flooding and draining experiment using spectral reflectance: Journal of Geophysical Research: Biogeosciences, 116, G00107, doi: 10.1029/2010JG001346.

Hall, D. L., S. M. Sterner, and R. J. Bodnar, 1988, Freezing-point depression of NaCl-KCl-H2O solutions: Economic Geology, 83, 197–202, doi: 10 .2113/gsecongeo.83.1.197.

Hauck, C., 2002, Frozen ground monitoring using DC resistivity tomography: Geophysical Research Letters, 29, 2016, doi: 10.1029/2002GL014995.

Hayashi, M., 2004, Temperature-electrical conductivity relation of water for environmental monitoring and geophysical data inversion: Environmental Monitoring and Assessment, 96, 119–128, doi: 10.1023/B:EMAS .0000031719.83065.68.

Hayley, K., L. R. Bentley, M. Gharibi, and M. Nightingale, 2007, Low temperature dependence of electrical resistivity: Implications for near surface geophysical monitoring: Geophysical Research Letters, 34, L18402, doi: 10.1029/2007GL031124.

Hinkel, K. M., J. A. Doolittle, J. G. Bockheim, F. E. Nelson, R. Paetzold, and J. M. Kimble, 2001, Detection of subsurface permafrost features with ground-penetrating radar, Barrow, Alaska: Permafrost and Periglacial Processes, 12, 179–190, doi: 10.1002/ppp.369.

Hinkel, K. M., and F. E. Nelson, 2003, Spatial and temporal patterns of active layer thickness at circumpolar active layer monitoring (CALM) sites in northern Alaska, 1995–2000: Journal of Geophysical Research: Atmospheres, 108, D28168., doi: 10.1029/2001JD000927.

Hinzman, L. D., N. D. Bettez, W. R. Bolton, F. S. Chapin, M. B. Dyurgerov, C. L. Fastie, B. Griffith, R. D. Hollister, A. Hope, H. P. Huntington, A. M. Jensen, G. J. Jia, O. Jorgenson, D. L. Kane, D. R. Klein, G. Kofinas, A. H. Lynch, A. H. Lloyd, A. David McGuire, F. E. Nelson, W. C. Oechel, T. E. Osterkamp, C. H. Racine, V. E. Romanovsky, R. S. Stone, D. A. Stow, M. Sturm, C. E. Tweedie, G. L. Vourlitis, M. D. Walker, D. A. Walker, P. J. Webber, J. M. Welker, K. S. Winker, and K. Yoshikawa, 2005, Evidence and implications of recent climate change in northern Alaska and other arctic regions: Climatic Change, 72, 251–298, doi: 10.1007/s10584-005-5352-2.

Hinzman, L. D., D. L. Kane, R. E. Gieck, and K. R. Everett, 1991, Hydrologic and thermal properties of the active layer in the Alaskan Arctic: Cold Regions Science and Technology, 19, 95–110, doi: 10.1016/0165-232X (91)90001-W.

Hivon, E. G., and D. C. Sego, 1993, Distribution of saline permafrost in the Northwest-Territories, Canada: Canadian Geotechnical Journal, 30, 506– 514, doi: 10.1139/t93-043.

Hivon, E. G., and D. C. Sego, 1995, Strength of frozen saline soils: Canadian Geotechnical Journal, 32, 336–354, doi: 10.1139/t95-034.

Hubbard, S. S., C. Gangodagamage, B. Dafflon, H. Wainwright, J. Peterson, A. Gusmeroli, C. Ulrich, Y. Wu, C. Wilson, J. Rowland, C. Tweedie, and S. D. Wullschleger, 2013, Quantifying and relating land-surface and subsurface variability in permafrost environments using LiDAR and surface geophysical datasets: Hydrogeology Journal, 21, 149–169, doi: 10.1007/ s10040-012-0939-y.

Hugelius, G., J. Strauss, S. Zubrzycki, J. W. Harden, E. A. G. Schuur, C.-L. Ping, L. Schirrmeister, G. Grosse, G. J. Michaelson, C. D. Koven, J. A. O'Donnell, B. Elberling, U. Mishra, P. Camill, Z. Yu, J. Palmtag, and P. Kuhry, 2014, Estimated stocks of circumpolar permafrost carbon with quantified uncertainty ranges and identified data gaps: Biogeosciences, 11, 6573–6593., doi: 10.5194/bg-11-6573-2014.

James, M. R., and S. Robson, 2012, Straightforward reconstruction of 3D surfaces and topography with a camera: Accuracy and geoscience application: Journal of Geophysical Research: Earth Surface, 117, F03017, doi: 10.1029/2011JF002289.

Johnson, T. C., L. D. Slater, D. Ntarlagiannis, F. D. Day-Lewis, and M. Elwaseif, 2012, Monitoring groundwater-surface water interaction using time-series and time-frequency analysis of transient three-dimensional electrical resistivity changes: Water Resources Research, 48W07506, doi: 10.1029/2012WR011893.

Jorgenson, M. T., 2011, Coastal region of northern Alaska: Guidebook to permafrost and related features: Department of Natural Resources.

Jorgenson, M. T., V. Romanovsky, J. Harden, Y. Shur, J. O’Donnell, T. Schuur, and M. Kanevskiy, 2010, Resilience and vulnerability of permafrost to climate change: Canadian Journal of Forest Research, 40, 1219– 1236., doi: 10.1139/ X10-060.

Kanevskiy, M., Y. Shur, M. T. Jorgenson, C. Ping, G. J. Michaelson, D. Fortier, E. Stephani, M. Dillon, and V. Tumskoy, 2013, Ground ice in the upper permafrost of the Beaufort Sea coast of Alaska: Cold Regions Science and Technology, 85, 56–70, doi: 10.1016/j.coldregions.2012.08 .002.

Karaoulis, M., A. Revil, D. D. Werkema, B. J. Minsley, W. F. Woodruff, and A. Kemna, 2011, Time-lapse three-dimensional inversion of complex conductivity data using an active time constrained (ATC) approach: Geophysical Journal International, 187, 237–251, doi: 10.1111/j.1365-246X .2011.05156.x.

Keller, G. V., and F. C. Frischknecht, 1966, Electrical methods in geophysical prospecting: Pergamon Press Inc..

Kemna, A., 2000, Tomographic inversion of complex resistivity — Theory and application: Ph.D. thesis, Bochum Ruhr University.

Kokelj, S. V., T. C. Lantz, S. A. Wolfe, J. C. Kanigan, P. D. Morse, R. Coutts, N. Molina-Giraldo, and C. R. Burn, 2014, Distribution and activity of ice wedges across the forest-tundra transition, western Arctic Canada: Journal of Geophysical Research: Earth Surface, 119, 2032–2047, doi: 10.1002/2014JF003085.

Koven, C. D., B. Ringeval, P. Friedlingstein, P. Ciais, P. Cadule, D. Khvorostyanov, G. Krinner, and C. Tarnocai, 2011, Permafrost carbon-climate feedbacks accelerate global warming: Proceedings of the National Academy of Sciences of the United States of America, 108, 14769–14774, doi: 10.1073/pnas.1103910108.

Krautblatter, M., S. Verleysdonk, A. Flores-Orozco, and A. Kemna, 2010, Temperature-calibrated imaging of seasonal changes in permafrost rock walls by quantitative electrical resistivity tomography (Zugspitze, German/Austrian Alps): Journal of Geophysical Research: Earth Surface, 115, F02003., doi: 10.1029/2008JF001209.

LaBrecque, D. J., M. Miletto, W. Daily, A. Ramirez, and E. Owen, 1996, The effects of noise on Occam’s inversion of resistivity tomography data: Geophysics, 61, 538–548, doi: 10.1190/1.1443980.

Lachenbruch, A. H., 1962, Mechanics of thermal contraction cracks and icewedge polygons in permafrost: GSA Special Papers, 70, 1–66, doi: 10 .1130/SPE70-p1.

Leffingwell, E., 1915, Ground-ice wedges, the dominant form of ground-ice on the north coast of Alaska: Journal of Geology, 23, 635–654, doi: 10 .1086/622281.

Mackay, J. R., 2000, Thermally induced movements in ice-wedge polygons, western Arctic coast: A long-term study: Geographie Physique Et Quaternaire, 54, 41–68, doi: 10.7202/004846ar.

Maidment, D. R., 1993, Handbook of hydrology: McGraw-Hill.

McCleskey, R. B., D. K. Nordstrom, J. N. Ryan, and J. W. Ball, 2012, A new method of calculating electrical conductivity with applications to natural waters: Geochimica et Cosmochimica Acta, 77, 369–382, doi: 10.1016/j .gca.2011.10.031.

McGinnis, L. D., D. K. Nakao, and C. C. Clark, 1973, Geophysical identification of frozen and unfrozen ground, Antarctica: Proceedings of the 2nd International Conference on Permafrost, National Academy of Sciences, 136–146.

McNeill, J. D., 1980, Electromagnetic terrain conductivity measurement at low induction numbers, Geonics, Technical NoteTN-6.

McNeill, J. D., 1990, Use of electromagnetic methods for groundwater studies, in S. Ward, ed., Geotechnical and environmental geophysics, vol. 1: SEG, 191–218.

Meyer, H., L. Schirrmeister, A. Andreev, D. Wagner, H.-W. Hubberten, K. Yoshikawa, A. Bobrov, S. Wetterich, T. Opel, E. Kandiano, and J. Brown, 2010, Late glacial and Holocene isotopic and environmental history of northern coastal Alaska — Results from a buried ice-wedge system at Barrow: Quaternary Science Reviews, 29, 3720–3735, doi: 10.1016/j .quascirev.2010.08.005.

Michaelson, G. J., C. L. Ping, and M. T. Jorgenson, 2011, Methane and carbon dioxide content in eroding permafrost soils along the Beaufort Sea coast, Alaska: Journal of Geophysical Research: Biogeosciences, 116, G01022, doi: 10.1029/2010JG001387.

Nicolsky, D. J., V. E. Romanovsky, N. N. Romanovskii, A. L. Kholodov, N. E. Shakhova, and I. P. Semiletov, 2012, Modeling sub-sea permafrost in the East Siberian Arctic Shelf: The Laptev Sea region: Journal of Geophysical Research: Earth Surface, 117, F03028, doi: 10.1029/ 2012JF002358.

Nicolsky, D., and N. Shakhova, 2010, Modeling sub-sea permafrost in the East Siberian Arctic Shelf: The Dmitry Laptev Strait: Environmental Research Letters, 5, 015006, doi: 10.1088/1748-9326/5/1/ 015006.

O’Sullivan, J., 1966, Geochemistry of permafrost, Barrow, Alaska: Proceedings of International Conference on Permafrost, National Academy of Sciences, 1287, 30–37.

Overduin, P. P., S. Westermann, K. Yoshikawa, T. Haberlau, V. Romanovsky, and S. Wetterich, 2012, Geoelectric observations of the degradation of nearshore submarine permafrost at Barrow (Alaskan Beaufort Sea): Journal of Geophysical Research: Earth Surface, 117, F02004., doi: 10 .1029/2011JF002088.

Pecheritsyna, S. A., V. A. Shcherbakova, A. L. Kholodov, V. N. Akimov, T. N. Abashina, N. E. Suzina, and E. M. Rivkina, 2007, Microbiological analysis of cryopegs from the Varandei Peninsula, Barents Sea: Microbiology, 76, 614–620, doi: 10.1134/S0026261707050153.

Ping, C.-L., G. J. Michaelson, M. T. Jorgenson, J. M. Kimble, H. Epstein, V. E. Romanovsky, and D. A. Walker, 2008, High stocks of soil organic carbon in the North American Arctic region: Nature Geoscience, 1, 615–619, doi: 10.1038/ngeo284.

Potter, R. W., M. A. Clynne, and D. L. Brown, 1978, Freezing-point depression of aqueous sodium-chloride solutions: Economic Geology, 73, 284– 285, doi: 10.2113/gsecongeo.73.2.284.

Pullman, E. R., M. T. Jorgenson, and Y. Shur, 2007, Thaw settlement in soils of the Arctic Coastal Plain, Alaska: Arctic Antarctic and Alpine Research, 39, 468–476.

Quinn, N. W. T., R. Ortega, P. J. A. Rahilly, and C. W. Royer, 2010, Use of environmental sensors and sensor networks to develop water and salinity budgets for seasonal wetland real-time water quality management: Environmental Modelling & Software, 25, 1045–1058, doi: 10.1016/j.envsoft .2009.10.011.

Revil, A., L. M. Cathles, S. Losh, and J. A. Nunn, 1998, Electrical conductivity in shaly sands with geophysical applications: Journal of Geophysical Research: Solid Earth, 103, 23925–23936., doi: 10.1029/ 98JB02125.

Romanovsky, V. E., and T. E. Osterkamp, 2000, Effects of unfrozen water on heat and mass transport processes in the active layer and permafrost: Permafrost and Periglacial Processes, 11, 219–239, doi: 10.1002/1099-1530(200007/09)11:33.0.CO;2-7.

Romanovsky, V. E., and T. E. Osterkamp, 2001, Permafrost: Changes and impacts, in R. Paepe, V. Melnikov, E. Van Overloop, and V. Gorokhov, eds., Permafrost response on economic development, environmental security and natural resources: Springer, NATO Science Series 76 , 297–315.

Schaefer, K., H. Lantuit, V. E. Romanovsky, and S. E. A. G., 2012, Policy implications of warming permafrost: United Nations Environment Programme, Special report.

Schaphoff, S., U. Heyder, S. Ostberg, D. Gerten, J. Heinke, and W. Lucht, 2013, Contribution of permafrost soils to the global carbon budget: Environmental Research Letters, 8, 014026, doi: 10.1088/1748-9326/8/1/ 014026.

Sellmann, P. V., J. Brown, R. I. Lewellen, H. McKim, and C. Merry, 1975, The classification and geomorphic implication of thaw lakes on the Arctic coastal plain: U.S. Army CRREL, Research report 344.

Shcherbakova, V. A., N. A. Chuvilskaya, E. M. Rivkina, S. A. Pecheritsyna, K. S. Laurinavichius, and N. E. Suzina, 2005, Novel psychrophilic anaerobic spore-forming bacterium from the overcooled water brine in permafrost: Description Clostridium algoriphilum sp. nov.: Extremophiles, 9, 239–246.

Shcherbakova, V. A., N. A. Chuvil’skaya, E. M. Rivkina, S. A. Pecheritsyna, S. V. Suetin, K. S. Laurinavichius, A. M. Lysenko, and D. A. Gilichinsky, 2009, Novel halotolerant bacterium from cryopeg in permafrost: Description of Psychrobacter muriicola sp. nov.: Microbiology, 78, 84–91, doi: 10 .1134/S0026261709010111.

Shiklomanov, N. I., D. A. Streletskiy, F. E. Nelson, R. D. Hollister, V. E. Romanovsky, C. E. Tweedie, J. G. Bockheim, and J. Brown, 2010, Decadal variations of active-layer thickness in moisture-controlled landscapes,

Barrow, Alaska: Journal of Geophysical Research: Biogeosciences, 115, G00I04, doi: 10.1029/2009JG001248.

Smith, M. J., J. Chandler, and J. Rose, 2009, High spatial resolution data acquisition for the geosciences: Kite aerial photography: Earth Surface Processes and Landforms, 34, 155–161, doi: 10.1002/esp.1702.

Tarnocai, C., J. G. Canadell, E. A. G. Schuur, P. Kuhry, G. Mazhitova, and S. Zimov, 2009, Soil organic carbon pools in the northern circumpolar permafrost region: Global Biogeochemical Cycles, 23, GB2023., doi: 10.1029/2008GB003327.

Velli, Y. Y., and P. A. Grishin, 1983, On the functional dependence of the freezing point of soils on the composition of water soluble salts in an interstitial solution, in Rheology of soils and engineering geocryology (translated from Russian), Canada Institute for Scientific and Technical Information, National Research Council of Canada, 193–196.

Visconti, F., J. M. de Paz, and J. L. Rubio, 2010, An empirical equation to calculate soil solution electrical conductivity at 25 degrees C from major ion concentrations: European Journal of Soil Science, 61, 980–993, doi: 10.1111/j.1365-2389.2010.01284.x.

Washburn, A. L., 1979, Geocryology: Edward Arnold.

Washburn, A. L., 1980, Permafrost features as evidence of climatechange: Earth-Science Reviews, 15, 327–402, doi: 10.1016/0012-8252 (80)90114-2.

Williams, J. R., 1970, Ground water in the permafrost regions of Alaska : Ground water in permafrost regions in Alaska occurs according to the same geologic and hydrologic principles prevailing in temperate regions: U.S. Survey.

Wu, Y., S. S. Hubbard, C. Ulrich, and S. D. Wullschleger, 2013, Remote monitoring of freeze-thaw transitions in arctic soils using the complex resistivity method: Vadose Zone Journal, 12, no. 1, doi: 10.2136/ vzj2012.0062.

Yoshikawa, K., C. Leuschen, A. Ikeda, K. Harada, P. Gogineni, P. Hoekstra, L. Hinzman, Y. Sawada, and N. Matsuoka, 2006, Comparison of geophysical investigations for detection of massive ground ice (pingo ice): Journal of Geophysical Research: Planets, 111, E06S19, doi: 10.1029/ 2005JE002573.

Yoshikawa, K., V. Romanovsky, N. Duxbury, J. Brown, and A. Tsapin, 2004, The use of geophysical methods to discriminate between brine layers and freshwater taliks in permafrost regions: Journal of Glaciology and Geocryology, 26, 301–309.